



On the development and analysis of coupled surface–subsurface models of catchments. Part 3. Analytical solutions and scaling laws

Piotr Morawiecki^{1,†} and Philippe H. Trinh^{1,†}

¹Department of Mathematical Sciences, University of Bath, Bath BA2 7AY, UK

(Received 3 November 2022; revised 27 November 2023; accepted 28 November 2023)

The objective of this three-part work is to formulate and rigorously analyse a number of reduced mathematical models that are nevertheless capable of describing the hydrology at the scale of a river basin (i.e. catchment). Coupled surface and subsurface flows are considered. In this third part, we focus on the development of analytical solutions and scaling laws for a benchmark catchment model that models the river flow (runoff) generated during a single rainfall. We demonstrate that for catchments characterised by a shallow impenetrable bedrock, the shallow-water approximation allows a reduction of the governing formulation to a coupled system of one-dimensional time-dependent equations for the surface and subsurface flows. Asymptotic analysis is used to derive semi-analytical solutions for the model. We provide simple asymptotic scaling laws describing the peak flow formation, and demonstrate its accuracy through a comparison with the two-dimensional model developed in Part 2. These scaling laws can be used as an analytical benchmark for assessing the validity of other physical, conceptual or statistical models of catchments.

Key words: river dynamics, shallow water flows

1. Introduction

In this third and final part of our work, we leverage the parametric study (Part 1: Morawiecki & Trinh 2024*a*) and two-dimensional (2-D) benchmark models (Part 2: Morawiecki & Trinh 2024*b*) to perform an in-depth asymptotic analysis of a coupled surface–subsurface model of a catchment. We specifically focus on flow within an aquifer characterised by a thin porous layer. The system begins in a steady state, for a constant

† Email addresses for correspondence: piotr.morawiecki@bath.edu, p.trinh@bath.ac.uk

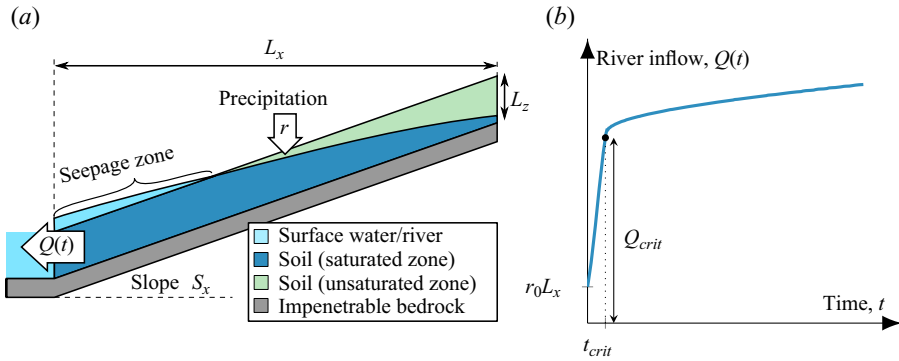


Figure 1. (a) Studied hillslope geometry; initially groundwater and surface water are in steady state for precipitation rate r_0 , and therefore river inflow (per unit length) is $Q(0) = r_0 L_x$. The simulated rise of river inflow caused by a constant rainfall $r > r_0$ is presented in (b). Note the characteristic fast rise of the river inflow to Q_{crit} at $t \in [0, t_{crit}]$.

precipitation r_0 , which is characterised by an initial seepage zone. Our objective is to understand the response of the catchment, when subjected to intense rainfall $r > r_0$.

One of the main conclusions from the numerical simulations in Part 2 is that in early time, the river inflow rapidly increases as a result of the rainfall accumulating over the initial seepage zone. It eventually reaches a critical flow, followed by a much slower rise in the river inflow caused by the expansion of the seepage zone (see figure 1). One of the primary results we derive in this work, is an analytical solution for both early and late times, including a simple analytical formula for the critical flow:

$$Q_{crit} = \underbrace{K_s S_x L_z}_{\text{groundwater flow}} + r L_x \underbrace{\left(1 - \frac{K_s S_x L_z}{r_0 L_x}\right)}_{\text{overland flow}}. \quad (1.1)$$

This formula consists of a contribution from the groundwater flow, and a contribution from the overland flow formed over the seepage zone. The parameters L_x , L_z and S_x relate to geometrical features of the hillslope, K_s corresponds to the soil hydraulic conductivity, whereas r_0 and r represent the initial and simulated rainfall intensity, respectively.

We argue that such analytical scaling laws are valuable, both as a tool to diagnose the correctness of other, more complex rainfall-runoff models, and also as a measure for characterising a catchment's propensity to flooding.

The introduction of Part 1 covers the general subject of hydrology and parameter estimation, whereas the introduction of Part 2 covers computational rainfall-runoff models. We begin by discussing the content of this current paper, focusing on asymptotics and scaling laws, in the context of the existing literature.

1.1. On the importance of analytical benchmarks results

Catchment hydrology is one of many areas of engineering where numerical approaches tend to dominate over analytical ones. Due to the complex multiscale nature of hydrology, limited data availability and high computational cost, formulating and solving the correct equations can be enormously challenging (Grayson, Moore & McMahon 1992). Instead of the physical models based on the fundamental laws of hydrodynamics, simpler models such as conceptual and statistical models are often used instead (Moore *et al.* 2007).

They are usually developed following a trial-and-error approach to fit available real-world data. However, these models do not provide any guarantee of model performance when applied to situations that may be underrepresented or missing in the training datasets (Parkin *et al.* 1996; Bathurst *et al.* 2004; Beven 2018).

To better understand the theoretical limits of different classes of catchment models, it is crucial to have a solid understanding of the different processes characterising the physical models. This goal can be achieved by developing numerical benchmark scenarios, as done by, e.g. Sulis *et al.* (2010) and Maxwell *et al.* (2014), and using them to compare predictions of different models. One perspective is that, in order to ensure consistency between the models over a wide range of input parameters, models should predict the same scaling laws for key features. For example, if one model predicts that the peak river flow, Q , is proportional to the catchment area, A , so $Q \propto A$, whereas another model predicts that $Q \propto \sqrt{A}$, then regardless of the fitting of these models, they cannot give consistent predictions over the entire range of A values. For example, the second model fitted to a training dataset dominated with measurements conducted in large catchments would tend to overestimate flow in the case of small, often ungauged, catchments.

The above perspective may seem oversimplistic. However, we argue that despite many statistical works demonstrating such scaling laws (cf. Cunnane 1987; Kjeldsen, Jones & Bayliss 2008) the comparison of asymptotic scaling laws between different catchment models is not a commonly used approach in the modern hydrology (although see Vieira (1983) for a comparison of Saint Venant approximations, and Cook, Knight & Wooding (2009) for comparison of Richards and Boussinesq-based models).

The emphasis of our work, here, on deriving of such analytical scaling laws for flow prediction in the case of coupled surface–subsurface flows in catchments. Not only do these scaling laws provide clear guidance on the key dependencies of model parameters, but their analysis often illuminates further model simplifications.

Next, we provide a brief overview of the existing analytical theory, highlighting the lack of research on fully coupled surface–subsurface systems.

1.2. *On analytical solutions in catchment hydrology*

The typical governing equations used in physical catchment models include Richards equation for the subsurface flow (or the Boussinesq equation for the unconfined groundwater flow) and the Saint Venant equations for the overland and channel flows (see, e.g. the review by Shaw *et al.* 2010). These equations and their simplifications have been well-studied using analytical methods, although largely in an uncoupled manner. One of the equations studied is the Boussinesq equation, which is commonly used to determine the shape of the groundwater table. In this paper by Boussinesq equation we refer to the Boussinesq equation used to describe unconfined groundwater flow (see, e.g. Hálek & Švec 2011, chap. 2; Troch *et al.* 2013), in order to distinguish it from other equations and approximations known by the same name. In some cases, analytical solutions for this equation can be derived. Examples include for example steady-state groundwater flow and evolution in one-dimensional (1-D) hillslopes (Polibarinova-Kochina & Wiest 1962; Troch *et al.* 2013). Similarly, analytical solutions have been developed for the 1-D Richards equation to describe water transfer through the unsaturated soil under constant and time-varying infiltration (Warrick, Lomen & Islas 1990).

For the case of overland flow over a hillslope, analytical solutions have been found for a kinematic approximation of the Saint Venant equations, as done, e.g. by Parlange, Rose & Sander (1981) and Tao, Wang & Lin (2018). These analytical solutions and their

approximations are important as they provide benchmark models for testing numerical schemes (e.g. benchmarks by MacDonald *et al.* (1995) for the overland flow and by Tracy (2006) for the subsurface flow), and can be used to develop less computationally demanding modelling approaches such as TOPMODEL by Kirkby & Beven (1979). However, no analytical solutions have been found so far coupled systems that include governing equations describing both subsurface/groundwater and surface flow. Despite the importance of these models in catchment hydrology, the study of these models has been restricted to numerical solutions only (Maxwell *et al.* 2014).

1.3. *On the shallow-water approximation for subsurface flow*

Previously, in Part 2, we introduced deep-aquifer scenario to describe a catchment with a deep aquifer, and shallow-aquifer scenario to describe a catchment where the subsurface flow is predominantly transferred through a thin porous layer near the surface. Mathematically, shallow-aquifer scenario is the limiting case of deep-aquifer scenario in which the aquifer depth is much smaller than the catchment width, $L_z \ll L_x$. We showed that in both cases, under standard initial conditions, the full three-dimensional (3-D) catchment model can be reduced to a simpler 2-D hillslope model. We shall begin with this 2-D assumption as the basis in this paper. We then demonstrate that in the shallow-water scenario, under certain assumptions, the 2-D model can be further reduced to a 1-D model.

The reduction of the 2-D subsurface flow into a 1-D model is not a new concept. The simplification is based on the Dupuit–Forchheimer approximation by Dupuit (1863) and Forchheimer (1914), which states that the groundwater flow is predominantly horizontal, and that the total flow scales proportionally with the saturated aquifer thickness. Boussinesq (1877) used this assumption to develop a 1-D model for the groundwater height; this is now known as the Boussinesq equation for groundwater flow (see, e.g. Bartlett & Porporato 2018), or the Dupuit–Boussinesq equation (see, e.g. Guérin, Devauchelle & Lajeunesse 2014). As we show later, it can be derived from the 2-D Richards model under the aforementioned assumption that $L_z \ll L_x$. The accuracy of this approximation is studied in detail by Paniconi *et al.* (2003) and Cook *et al.* (2009).

The Boussinesq equation is commonly used in groundwater modelling, and a wide class of analytical and approximate solutions has been developed. Notable examples are reviewed by Wooding & Chapman (1966), Anderson & Brooks (1996), Troch, Paniconi & Emiel van Loon (2003) and Bartlett & Porporato (2018). These studies, however, concern only groundwater flow, and do not involve the coupling with the overland flow, which is an essential component of a standard physical catchment model.

Here, we extend these studies by including the effect of overland flow in the Boussinesq equation. Our main result in this paper is the derivation and analysis of the following 1-D dimensionless coupled surface/subsurface model:

$$\frac{\partial H}{\partial t} = \begin{cases} f(x)^{-1} \left[\frac{\partial}{\partial x} \left(\sigma H \frac{\partial H}{\partial x} + H \right) + \rho_0 r(x, t) \right] & \text{if } H \leq 1, \\ \frac{\partial}{\partial x} \left(\sigma \frac{\partial H}{\partial x} + \mu (H - 1)^k \right) + \rho_0 r(x, t) & \text{if } H > 1, \end{cases} \quad (1.2)$$

where $f(x)$, σ , μ and ρ_0 are dimensionless parameters explained in detail in § 2, and $H(x, t)$ is the total height of groundwater and surface water, which depends on the distance from the channel x and time t . Values $H \leq 1$ represent unsaturated soil without surface water, and $H > 1$ represent saturated soil with surface water. The main difference from

the classical Boussinesq equation is the second case in the above equation with $H > 1$, in which we include an additional term representing the overland flow.

We use the above 1-D coupled surface–subsurface model to develop analytical solutions for the river flow formed by rainfall of a constant intensity (however, the result can be generalised for time-dependent rainfall). Our methodology takes advantage of the negligibly small size of the diffusion terms in most of the seepage zone, which allows us to use the method of characteristics for the study of wave propagation. This approach is similar to previous kinematic treatments of the Saint Venant equations (Henderson & Wooding 1964; Woolhiser & Liggett 1967), but for our problem, the size of the seepage zone increases as a result of rising groundwater, which introduces a secondary dynamics.

The analytical approximations we develop in this work are possible due to a few governing assumptions; they are supported by the analysis of the typical values of catchment parameters described in Part 1 (Morawiecki & Trinh 2024a). The main approximations are: (i) the typical rainfall duration is much shorter than the characteristic timescale of groundwater flow; (ii) the typical timescale of surface flow is much shorter than that of subsurface flow; and (iii) the mean precipitation rate is larger than the maximal groundwater flow passing through the saturated zone.

We start by introducing the above 1-D model in § 2, with its typical dynamics discussed in § 3. For a scenario of single intensive rainfall described in § 4, we find an approximated analytical form of the initial steady state in § 5, followed by a short-time asymptotic analysis in § 6. The accuracy of the developed analytical approximations is assessed in § 7. In § 8, we highlight key hydrograph features predicted by this analytical solution, followed by conclusions in § 9 and further discussion in § 10.

2. Formulation of the 1-D coupled model

In this section, we introduce a 1-D model describing the horizontal groundwater and overland flow along the hillslope, firstly in a dimensional and then in a dimensionless form. Its formal mathematical derivation from the 2-D benchmark model introduced in our previous paper is presented in Appendix B: here we focus on presenting the general structure of the model instead.

2.1. Dimensional model

Let us consider a 2-D hillslope of length L_x with a uniform terrain slope S_x , uniform thickness of the porous layer L_z , uniform saturated soil hydraulic conductivity K_s and an impenetrable bedrock beneath the hillslope. As shown in the (x, z) -plane in figure 2, we denote the thickness of the saturated zone as $H_g(x, t)$ and the height of the surface water as $h_s(x, t)$.

We shall assume that overland flow can only occur when the soil becomes fully saturated. The overland flow generated by exceeding the soil infiltration capacity (Kirkby 2019) is not considered. Under this assumption, the heights H_g and h_s can be combined to form a single dependent variable,

$$H(x, t) = H_g(x, t) + h_s(x, t), \quad (2.1)$$

defined as the total height of groundwater and surface water. We now review the governing equations for H , for which the details are presented in Appendix B.

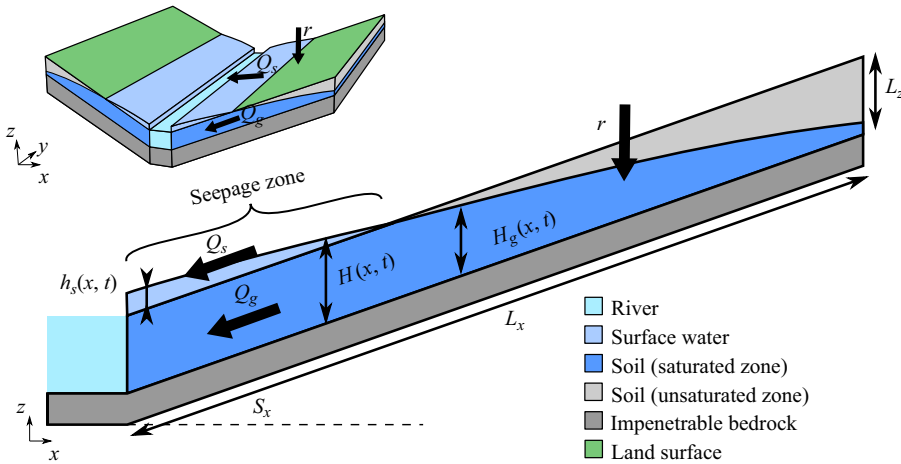


Figure 2. Hillslope geometry used to formulate a 1-D surface–subsurface model.

2.1.1. Groundwater flow

The standard approach to model shallow-water aquifers uses the Dupuit–Forchheimer assumption, which states that groundwater flows horizontally with the pressure head following a hydrostatic profile. Under this approximation, the groundwater flow is given by

$$Q_g = K_s H \frac{\partial H}{\partial x} + K_s H S_x. \tag{2.2}$$

When the soil is not fully saturated, and hence $H < L_z$, the evolution of the groundwater depth is given by the continuity equation, resulting in a standard form of the Boussinesq equation (Troch *et al.* 2013) for an unconfined aquifer:

$$f(x, t) \frac{\partial H_g}{\partial t} = \frac{\partial}{\partial x} Q_g + r = \frac{\partial}{\partial x} \left(K_s H_g \frac{\partial H_g}{\partial x} + K_s H_g S_x \right) + r(x, t), \tag{2.3}$$

where $r(x, t)$ denotes the groundwater recharge, and $f(x, t)$ is a drainable porosity. In this paper, we assumed that the recharge is equal to the precipitation.

The drainable porosity function is more subtle; as introduced in Appendix C, it is formally defined as the rate of change of groundwater volume, \mathcal{V} , given a change in the groundwater level, H , i.e. $f = d\mathcal{V}/dH$. Note that f depends on the soil saturation above the groundwater table. For example, higher soil saturation implies that less water is required to raise the groundwater by a given volume and, hence, f is lower. Recall that the soil saturation, θ , is computed as a function of the pressure head, h_g , as given by the Mualem–van Genuchten model (C3). In theory, computing f would involve coupling equation (2.3) with a model for $h_g(x, z, t)$.

In the literature (e.g. Troch *et al.* 2003), f is often assumed to be a parameter with a value specific to the soil type at a given location. In practice, however, f can change over time. For example, during a rainfall, a characteristic wetting front forms, which slowly propagates from the surface towards the groundwater table (Caputo & Stepanyants 2008). In order for this table to rise, the rainwater must first infiltrate through the unsaturated zone. This causes f to significantly change over time.

In this paper, we approximate $f(x, t)$ by a time-independent mean drainable porosity $f_{mean}(x)$. Although the model results will not duplicate the full time-dependent behaviour

observed in Part 2, the mean value, $f_{mean}(x)$, is chosen such that solutions correctly capture the key time when the groundwater reaches the land surface. We show later that the resultant model reproduces the hydrograph during a single precipitation event (see figure 9 later).

In Appendix C, we justify the choice of

$$f(x, t) \approx f_{mean}(x) \equiv \frac{v_H(x)}{D(x)}, \tag{2.4}$$

where $v_H(x)$ is the initial drainable volume per unit area at a given location, and $D(x) = L_z - H(x)$ is the depth of the groundwater below the land surface. In other words, the drainable porosity is given by the fraction of the soil volume that can be filled with water. Henceforth, we take the mean approximation (2.4) as the definition of f . Further discussion of the drainable porosity function is provided in Appendix C, where we provide formulae for its implementation.

2.1.2. Coupling with the overland flow

Now let us consider the case where the soil is fully saturated, for which $H_g = L_z$, which implies $H > L_z$. In this case, as derived in Appendix B, the surface depth h_s evolves according to the following continuity equation:

$$\frac{\partial h_s}{\partial t} = \frac{\partial}{\partial x}(Q_g + Q_s) + r = \frac{\partial}{\partial x} \left(K_s L_z \frac{\partial h_s}{\partial x} + \frac{\sqrt{S_x}}{n_s} h_s^k \right) + r(x, t). \tag{2.5}$$

In the above equation, we have used Manning’s equation to represent the overland flow:

$$Q_s = \frac{\sqrt{S_f}}{n_s} h_s^k \sim \frac{\sqrt{S_x}}{n_s} h_s^k, \tag{2.6}$$

where $k = 5/3$ and n_s is the Manning roughness coefficient, which depends on the hillslope surface type and is determined empirically. We use the kinematic approximation ($S_f \sim S_x$), where the friction slope S_f is only dependent on the elevation gradient S_x . Alternatively, we could also consider the diffusive approximation $S_f \sim S_x + \partial h_s / \partial x$; however, we limit this study to the kinematic approximation only for simplicity.

Furthermore, we note that apart from the constant gravitationally-induced groundwater flow, the pressure difference caused by the gradient of surface water height may affect the groundwater flow. Typically, the size of the overland flow is negligibly small compared with the thickness of the porous layer. However, as we discuss in § 5, this approximation fails at the propagating seepage front, which requires us to include the $(\partial/\partial x)(K_s L_z (\partial h_s / \partial x))$ diffusion term.

Now, we can combine (2.3) and (2.5) into a single equation for H :

$$\frac{\partial H}{\partial t} = \begin{cases} f(x)^{-1} \left[\frac{\partial}{\partial x} \left(K_s H \frac{\partial H}{\partial x} + K_s H S_x \right) + r \right] & \text{if } H \leq L_z, \\ \frac{\partial}{\partial x} \left[K_s L_z \frac{\partial H}{\partial x} + \frac{\sqrt{S_x}}{n_s} (H - L_z)^k \right] + r & \text{if } H > L_z. \end{cases} \tag{2.7}$$

We assume a no-flow boundary condition at the catchment boundary ($x = L_x$). At the location of the river ($x = 0$), we assume that the river table is located at the same level as the overland water height (or at the surface if no overland flow is present). Therefore, at $x = 0$ we set $H_g = L_z$ and a (flat) free-surface condition for the overland flow, $\partial h_s / \partial x = 0$.

In addition, in this work, we study the time evolution of the above system assuming that it is initially in equilibrium for a given mean rainfall $r_0 < r$, and then subjected to a rainfall r for $t > 0$. Therefore, for the initial condition, we take the steady-state of equation of (2.7) for a given mean rainfall r_0 . The boundary and initial conditions are summarised shortly in § 2.3.

2.1.3. Channel flow

As was discussed in § 3.3 of Part 2, the total groundwater and overland flow that is reaching the riverbank form a channel flow. This flow can be described by 1-D Saint Venant equations. However, in this study, our focus is on studying the properties of river inflow from the hillslope, not the subsequent channel flow. Therefore, for the purpose of this study, we assume that the river height is constant, limited to the depth of the channel. Analysing how the river inflow propagates through the channel (or the entire drainage network) and how the drying of the channel affects the surface and subsurface flows can be interesting extensions of this study.

2.2. Non-dimensional model

The above model can be non-dimensionalised by taking $x = L_x x'$, $t = T_0 t'$, $H = L_z H'$ and $r = r_0 r'$. Here, $T_0 = L_x / (K_s S_x)$ is a characteristic timescale of the groundwater flow, chosen to balance the temporal term and the $\partial_x(K_s H S_x)$ term.

Once non-dimensionalised, our governing equations (2.7) become (after dropping primes)

$$\frac{\partial H}{\partial t} = \begin{cases} f(x)^{-1} \left[\frac{\partial}{\partial x} \left(\sigma H \frac{\partial H}{\partial x} + H \right) + \rho_0 r(x, t) \right] & \text{if } H \leq 1, \\ \frac{\partial}{\partial x} \left(\sigma \frac{\partial H}{\partial x} + \mu (H - 1)^k \right) + \rho_0 r(x, t) & \text{if } H > 1, \end{cases} \quad (2.8a)$$

and the dimensionless parameters σ , μ and ρ_0 are introduced shortly in § 2.3. In this work, we assume that the rainfall is constant and uniform, i.e. $r(x, t) = r = \text{constant}$, except for the initial jump from r_0 to $r > r_0$. However, we shall discuss in § 10 that our methodology can be applied in the case of time-dependent rainfall.

In combination with the governing equations (2.8a), we have to specify the dimensionless boundary conditions. First, at $x = 0$, we need to consider two situations. First, if a seepage zone exists for the initial r_0 , we set a free flow boundary condition,

$$H_x(0, t) = 0. \quad (2.8b)$$

However, as we shall demonstrate in § 3.1, if r_0 is low enough, initially the seepage does not exist. Then we assume that $H(x, t)$ representing groundwater is reaching the surface at $x = 0$, i.e.:

$$H(0, t) = 1. \quad (2.8c)$$

During a rainfall ($r > r_0$), the groundwater gradient at $x = 0$, which is initially negative, increases as the groundwater rises. The seepage starts to grow, when the when it becomes positive, which is when boundary condition (2.8c) is replaced with (2.8b).

At the right-hand edge, by the definition of a catchment, there is zero flow:

$$Q(1, t) = 0, \tag{2.8d}$$

where the dimensionless total flow, Q , is defined as

$$Q(x, t) = \begin{cases} H + \sigma H \frac{\partial H}{\partial x} & \text{if } H \leq 1, \\ 1 + \sigma \frac{\partial H}{\partial x} + \mu(H - 1)^k & \text{if } H > 1. \end{cases} \tag{2.9}$$

For the initial condition, $H(x, t = 0) = H_0(x)$, we take a steady state of (2.8a) for $r = 1$:

$$0 = \begin{cases} \frac{\partial}{\partial x} \left(\sigma H_0 \frac{\partial H_0}{\partial x} + H_0 \right) + \rho_0 & \text{if } H_0 \leq 1, \\ \frac{\partial}{\partial x} \left(\sigma \frac{\partial H_0}{\partial x} + \mu (H_0 - 1)^k \right) + \rho_0 & \text{if } H_0 > 1. \end{cases} \tag{2.10}$$

In this paper, we refer to this model (2.8) as the *1-D model*.

2.3. The non-dimensional parameters

In the first case of (2.8), we have introduced two key dimensionless parameters, defined as

$$\sigma = \frac{L_z}{L_x S_x} = \frac{\text{thickness of the porous layer}}{\text{elevation drop along the hillslope}}, \tag{2.11a}$$

$$\rho_0 = \frac{r_0 L_x}{L_z S_x K_s} = \frac{\text{precipitation flux}}{\text{maximum groundwater flux}}. \tag{2.11b}$$

Note that $\sigma \rightarrow \infty$ as the hillslope becomes increasingly flat. The parameter ρ_0 represents the ratio of the total precipitation rate (given by rL_x in $\text{m}^2 \text{s}^{-1}$) to the maximum possible groundwater flow for fully saturated soil (given by $L_z S_x K_s$ in $\text{m}^2 \text{s}^{-1}$). Introduction of the maximum groundwater discharge is a classic concept in hydrology, see, e.g. Horton (1936).

In the second case of (2.8), we have introduced an additional dimensionless parameter:

$$\mu = \frac{L_z^{k-1}}{K_s S_x^{1/2} n_s}. \tag{2.12}$$

We argue later in § 6.2 that the characteristic size of the overland flow scales as $L_s = \mu^{-1/k} L_z$. Following that section, we introduce a key dimensionless parameter to describe the dynamics in the seepage zone, namely the Péclet number:

$$Pe = \frac{\mu^{1/k}}{\sigma} = \frac{\frac{\sqrt{S_x} L_s^k}{n_s}}{K_s L_z \frac{L_s}{L_x}} = \frac{\text{convective overland flow}}{\text{diffusive effect of the groundwater flow}}. \tag{2.13}$$

In order to interpret Pe , we note that the numerator represents the second term on the right-hand side of (2.7) for $H > L_z$, representing convective effects. The denominator represents the size of the first term on the right-hand side of (2.7) for $H > L_z$, representing diffusive effects.

Based on median values of physical parameters used in the above equations provided in table 1, we have $\sigma \approx 10^{-2}$, $\rho_0 \approx 1.5$, $\mu \approx 10^7$ and $Pe \approx 10^5$. Consequently, our work primarily focuses on the limits of μ , $Pe \rightarrow \infty$, where convection dominates diffusion.

Parameter	Symbol	Mean value	Unit
Catchment width	L_x	616	m
Catchment depth	L_z	1	m
Hydraulic conductivity	K_s	10^{-4}	m s^{-1}
Mean precipitation rate	r_0	2.95×10^{-8}	m s^{-1}
Peak precipitation rate	r	2.36×10^{-7}	m s^{-1}
Hillslope gradient	S_x	0.075	—
Manning’s roughness coefficient	n_s	0.051	$\text{s m}^{-1/3}$

Table 1. Typical values of physical parameters characterising UK catchments extracted in Part 1 of this paper (Morawiecki & Trinh 2024a).

3. Numerical methodology and typical dynamics

Recall that the solutions are essentially characterised by the overland and groundwater heights, and a quadruplet of parameters:

$$H = H(x, t; \sigma, \mu, \rho_0, r), \tag{3.1}$$

as well as the constant $k = 5/3$ appearing in Manning’s formula. These solutions are found by solving the partial differential equation (PDE) (2.8a) subject to the boundary conditions (2.8b)–(2.8d). In the typical configuration, the flow transitions from overland ($H > 1$) to groundwater ($H \leq 1$) at a contact point $x = a(t)$, which is determined as part of the solution.

The model in (2.8a) was implemented in Matlab using the ode15s solver to find its steady state and pdepe to solve the time-dependent problem. We divide the spatial and temporal domain as follows:

$$x_i = \frac{i}{N_x} \quad \text{and} \quad t_j = \frac{j}{N_t} t_{max}, \quad i, j = 1, 2, 3, \dots, \tag{3.2}$$

where we typically use $N_x = 200$ and $N_t = 300$. We check whether increasing mesh size and time resolution does not significantly affect the obtained solution, and if it does, we refine the mesh. The codes used to generate figures in this work are available in a GitHub repository (Morawiecki 2022). All numerical results in this paper were obtained for the values presented in table 1, unless stated otherwise.

3.1. Typical results for $\rho_0 < 1$ and $\rho_0 > 1$

The existence of the seepage zone in the initial steady state depends on whether the value of ρ_0 , defined in (2.11b), is higher or lower than 1, and each case exhibits a different transient behaviour. Typical solutions obtained in these two cases are shown in figure 3.

First, consider figure 3(a,b). In the case of $\rho_0 > 1$, we already have a seepage zone in the initial state. In a short timescale, the height of the surface water increases quickly until reaching a seemingly quasi-static state. Afterwards, the flow continues to increase as a result of the saturation front propagating uphill, but this process is characterised by a much longer timescale and a slower rate of flow rise. The difference between the short- and long-time behaviour can also be seen in the produced hydrograph in figure 4. It shows the dependence between the total river inflow, defined as the total flow (2.9) evaluated at

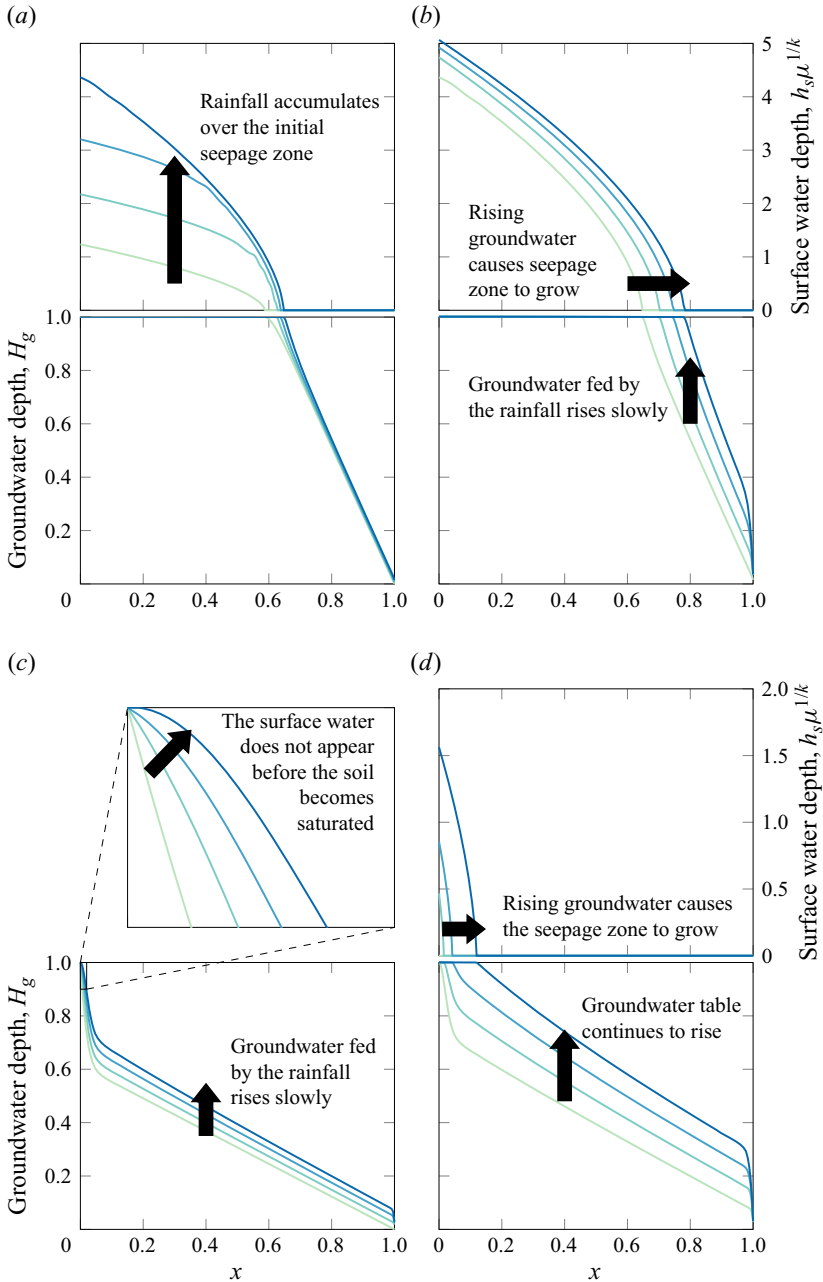


Figure 3. Schematic presenting early- and late-time dynamics for a catchment with and without an initial seepage zone (corresponding to $\rho_0 > 1$ and $\rho_0 \leq 1$ respectively). In (a), (b) and (c) a seepage zone is observed, and therefore a separate graph is presented to illustrate the evolution of the surface water depth (note that the vertical axis is multiplied by the scaling factor $\mu^{1/k} \approx 3260$).

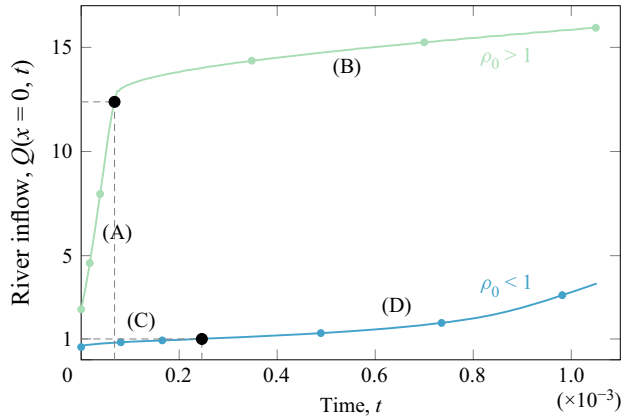


Figure 4. Schematic representation of the hydrograph obtained for a catchment with and without an initial seepage zone (corresponding to $\rho_0 > 1$ and $\rho_0 \leq 1$, respectively). Points represent times for which the profiles are shown in figure 3, whereas letters A–D refer to corresponding phases from that figure.

the river bank ($x = 0$),

$$Q(t) = Q(x = 0, t). \tag{3.3}$$

In the presented hydrograph, we have marked the initial fast transition as (A) and the subsequent slow transition as (B).

For $\rho_0 < 1$, we do not observe an initial seepage zone, i.e. $H(x, t = 0) < 1$ for all x . For some time the groundwater table is rising, increasing groundwater flow reaching the river, until the groundwater depth gradient at $x = 0$ becomes 0. Then the seepage zone starts to slowly form and propagate away from the channel, increasing the overland flow reaching the river.

However, in practice, in the case of real-world catchments characterised by a thin porous layer (which is a base assumption behind the presented 1-D model), the groundwater flow rate is highly limited. Therefore, in such catchments, we expect the $\rho_0 > 1$ case to be more prevalent, which is additionally confirmed by low base flow index (BFI) values characterising low-productive catchments. (BFI describes the ratio between the base flow and total flow in the given catchment. High values refer to catchments dominated by the groundwater flow, whereas low values refer to catchments with a significant overland flow component.) Therefore, in this paper, we focus on discussing the mathematical properties of each phase presented in figure 4 only in the case of $\rho_0 > 1$.

In general, the solution for the PDE model (2.8a) can only be found numerically. However, by taking advantage of the typical sizes of dimensionless parameters, the model can be further simplified. Figure 5 shows the effect of dimensionless parameters, ρ , ρ_0 , σ and μ on the model's solution. The graphs in the left column show how the initial steady state $H_0(x)$ depends on the value of each parameter, whereas the graphs on the right present the effect of each parameter on the hydrograph $Q(x = 0, t)$. The conclusions from this numerical experiment are as follows.

- (i) Parameter ρ_0 (typical value 2), which following (2.11b) characterises the mean precipitation rate in terms of the groundwater flow, has a significant effect on the initial steady state. As discussed in detail previously, $\rho_0 < 1$ corresponds to a hillslope with no initial seepage zone, and is characterised by different dynamics

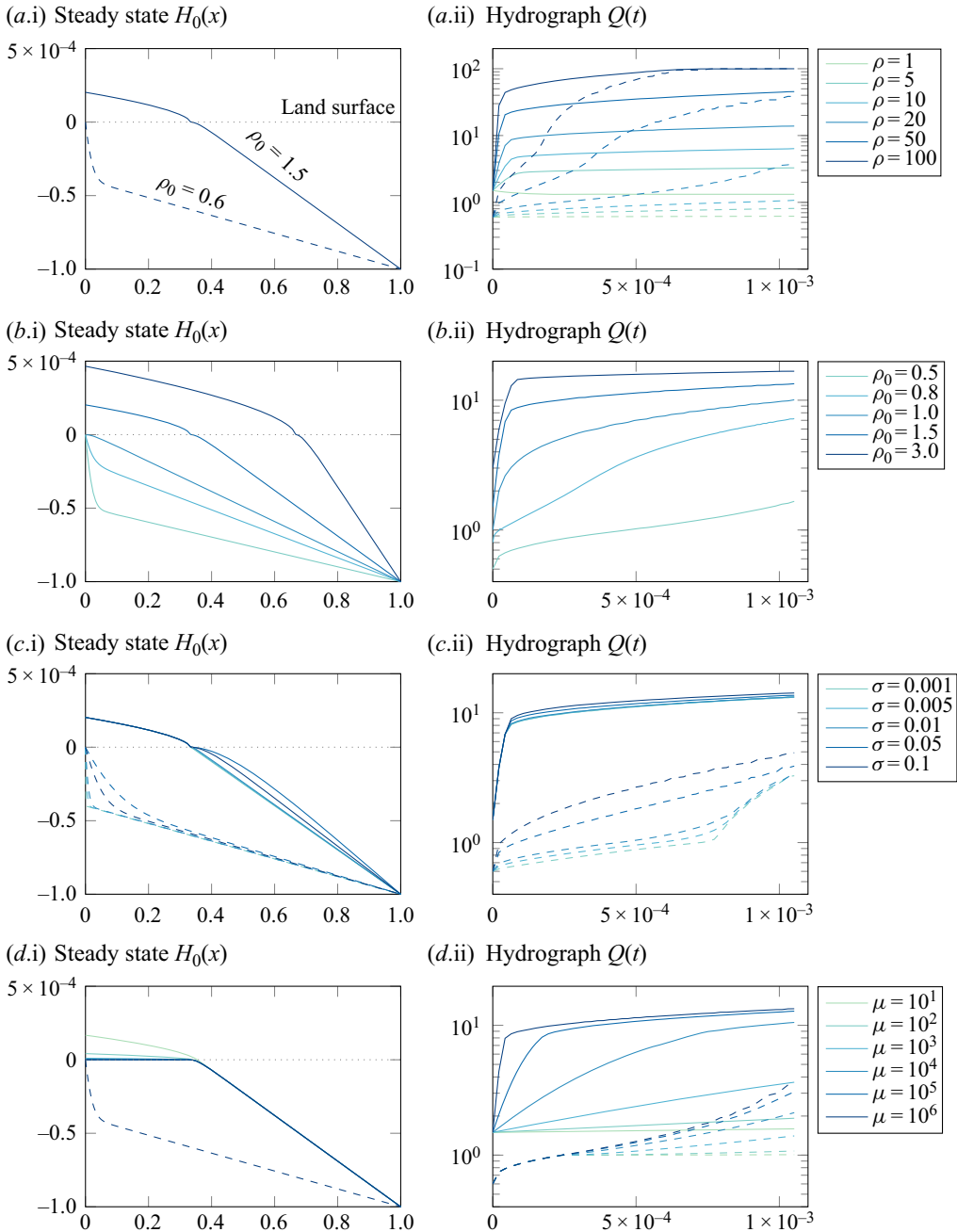


Figure 5. Effect of dimensionless parameters shown for the initial steady state $H_0(x)$ versus x (insets left column) and for the hydrograph $Q(t)$ versus t (insets right column). Inset (a) shows changing ρ_0 ; inset (b) shows changing ρ ; inset (c) shows changing σ ; and inset (d) shows changing μ . In the case of (a), (c) and (d), solid lines represent solutions for $\rho_0 = 1.5$ (scenario with an initial seepage zone), and dashed lines represent solutions for $\rho_0 = 0.6$ (scenario without an initial seepage zone). The surface water ($H > 0$) is magnified 1000 times.

than the $\rho_0 > 1$ case, in which we observe a fast rise of flow in the early time. In most of this paper, we consider only the latter case.

- (ii) Parameter ρ (typical value ≈ 20), which characterises the simulated precipitation rate in terms of the groundwater flow, does not affect the initial steady state, but it does affect how quickly the flow is rising. Higher ρ values lead to both a higher flow over the seepage zone and a faster growth of this zone. Values of ρ can vary significantly depending on the rainfall event considered.
- (iii) Parameter σ (typical value 10^{-2}), which following (2.11a) characterises the thickness of porous layer compared with the elevation drop along the hillslope, has a significant effect only on the solution outside the seepage zone. In the case of the seepage zone, the term including σ is negligibly small compared with the μ term. However, it affects the speed at which the seepage zone is growing. Note that as $\sigma \rightarrow 0$, the initial groundwater shape becomes a linear function (with a possible small boundary layer at its left border). Even though this limit is not critical in our analysis, it may allow us to approximate the initial groundwater shape without the need to solve the governing equations numerically.
- (iv) Parameter μ (typical value 10^6), which following (2.12) characterises the overland flux, does not have a significant effect on the groundwater table outside the seepage zone, but it has a major effect on the height of the surface water within the seepage zone. Higher μ values correspond to lower surface water height, which in the limit $\mu \rightarrow \infty$ becomes negligible compared with the variation of the groundwater depth. In addition, in this limit, the seepage zone size reaches a limiting value, $a_0 = 1 - 1/\rho_0$ (see § 5). This limit is strongly supported by real-world data (typical value of μ for UK catchments is of the order of 10^6 based on the typical parameter values estimated in Part 1 of this study), and it allows us to derive the formula for a typical hydrograph.

4. The formulation of an asymptotic model for intense rain

In the previous section, we presented numerical simulations of the full PDE system (2.8) and showed that under certain parameter choices, the resulting hydrographs could be approximately classified into two behaviours as shown in figure 3. In particular, when the system is initiated with an initial seepage zone, i.e. $\rho_0 > 1$, then in response to an intense rainfall with $r > 1$, the river inflow rapidly increases over time. It is important to note that the duration of a standard intensive rainfall is much shorter compared with the typical timescale of the groundwater flow (i.e. typical travel time along the hillslope), which is approximately

$$T_0 = \frac{L_x}{K_s S_x} \approx 1000 \text{ days.} \tag{4.1}$$

Our focus is to develop the short-time asymptotics to better understand this crucial response. Ultimately, we aim to derive an analytical solution for the river inflow, $Q(x = 0, t)$. Based on the physical constraints, we are primarily interested in the following asymptotic limits:

$$\left. \begin{aligned} \text{small-time : } & t \ll 1, \\ \text{convection-dominated flow in the seepage zone : } & Pe \gg 1, \\ \text{intense rainfall : } & \rho = r\rho_0 \gg 1. \end{aligned} \right\} \tag{4.2}$$

To begin, let us reformulate the governing system in terms of a boundary value problem. We assume that there exists a single contact line located at $x = a(t)$ where $H(a(t), t) = 1$. This configuration is illustrated in figure 2. From (2.8a), the evolution of these surfaces is governed by

$$\frac{\partial H}{\partial t} = \begin{cases} \frac{\partial}{\partial x} \left(\sigma \frac{\partial H}{\partial x} + \mu(H - 1)^k \right) + \rho & \text{for } x \in [0, a(t)], \quad (4.3a) \\ f(x)^{-1} \left[\frac{\partial}{\partial x} \left(\sigma H \frac{\partial H}{\partial x} + H \right) + \rho \right] & \text{for } x \in [a(t), 1]. \quad (4.3b) \end{cases}$$

Here, we have introduced $\rho = \rho_0 r$. Thus, we have a set of two time-dependent equations for H that are second-order in space, along with an additional contact-line position $a(t)$. Consequently, we require five boundary conditions in addition to the initial condition. Two boundary conditions are needed at $x = 0, 1$, and three matching conditions are required at the interface, $x = a(t)$. In total, these conditions are

$$\partial_x H(0, t) = 0, \quad \partial_x H(1, t) = -\sigma^{-1}, \quad (4.4a,b)$$

$$H(a^-, t) = 1, \quad H(a^+, t) = 1, \quad \partial_x H(a^-, t) = \partial_x H(a^+, t), \quad (4.4c-e)$$

where a^\pm corresponds to the right/left limits as $x \rightarrow a$.

The first two boundary conditions are obtained from (2.8b) and (2.8d). The next two boundary conditions arise from defining a as the point where the groundwater table reaches the surface (i.e. where $H = 1$). The last interface condition is a consequence of the continuity of flow given by (2.9). Note that a kinematic condition can be derived for the front position. Applying the chain rule to $H(a(t), t) = 1$, we have

$$\frac{\partial H}{\partial t} + \frac{\partial H}{\partial x} \frac{da}{dt} = 0 \quad \text{at } x = a(t). \quad (4.5)$$

Following (2.10), we set the initial condition given by the steady state of (4.3a)–(4.3b) for $r = 1$, which we denote as $H_0(x; \rho_0)$. Thus, H_0 satisfies

$$0 = \begin{cases} (\sigma H_0 H_0' + H_0)' + \rho_0 & \text{for } x > a(t = 0), \\ (\sigma H_0' + \mu(H_0 - 1)^k)' + \rho_0 & \text{for } x \leq a(t = 0), \end{cases} \quad (4.6)$$

where primes ($'$) denote differentiation with respect to x . Here, $a(t = 0)$ can be regarded as an eigenvalue and determined from this initial condition.

In the next two sections, we use this model to derive an asymptotic solution for the hydrograph $Q(t)$. Our approach involves three main steps.

- (i) First, in § 5, we study the initial state $H(x, 0) = H_0(x; r = 1)$, which is assumed to be the steady-state response to the rain input $r = 1$. This is a complicated coupled overland–groundwater problem, but we are able to develop analytical approximations in the limit of $\mu \rightarrow \infty$ or equivalently $Pe \rightarrow \infty$.
- (ii) Next, in § 6.1, we study the small-time response of the groundwater configuration and the propagation of the seepage zone relative to this initial steady state. At the time $t = 0$, the rainfall is set to $r > 1$, which causes the groundwater to rise and the seepage zone to shift. Analytical approximations can be developed for the case of $Pe \rightarrow \infty$ and for large rainfalls, $r \rightarrow \infty$.
- (iii) Finally, in § 6.2, we develop an analytical approach for predicting the evolution of the overland flow, which leverages our analysis of the seepage zone propagation

obtained in step (ii). This turns out to be a wave propagation study using the method of characteristics.

5. Asymptotic analysis of the initial condition, H_0 , with $Pe \rightarrow \infty$

In our model, we assume that the system begins at the configuration that corresponds to the particular steady-state solution forced by the ‘typical’ rainfall, ρ_0 .

By integrating (4.6) and applying the upstream boundary condition $q(1) = 0$, we obtain

$$\rho_0(1 - x) = \begin{cases} H_0 + \sigma H_0 H'_0 & \text{for } x > a, \\ 1 + \sigma H'_0 + \mu(H_0 - 1)^k & \text{for } x \leq a. \end{cases} \tag{5.1a}$$

$$\tag{5.1b}$$

The fact that the limit $\mu \rightarrow \infty$ involves the Péclet number, defined as $Pe = \mu^{1/k}/\sigma$ via (2.13), is not entirely obvious. Note that as $\mu \rightarrow \infty$, the dominant balance in the overland equation for $x \leq a$ indicates that $H_0 \sim 1$ in this limit. We rescale $x = aX$ and $H_0 = \mu^{-1/k}g(X)$, obtaining, for $X \in [0, 1]$,

$$\frac{Pe^{-1}}{a} \frac{\partial g}{\partial X} + g^k = \rho_0(1 - aX) - 1, \tag{5.2}$$

$$g'(0) = 0 \quad \text{and} \quad g(1) = 0. \tag{5.3}$$

In the limit $Pe \rightarrow \infty$, we note that naively, the diffusion term in (5.2) tends to zero. Then, since $g(1) = 0$, we can approximate $\rho(1 - a) \sim 1$, which gives the front position as $a \sim 1 - 1/\rho_0$. However, note that in this limit, the leading (outer) solution is given by $g \sim [\rho_0(1 - aX) - 1]^{1/k}$ and, hence, exhibits an infinite gradient as $X \rightarrow 1$. Consequently, it is not obvious that the diffusion term can be neglected *a priori* as $Pe \rightarrow \infty$. The gradient of the solution exhibits a boundary layer and thus requires a matched asymptotics approach.

In Appendix D, we show that the contact line, $x = a$, and the gradient at the front can be expanded into an asymptotic expansion. In terms of the original H_0 , this is

$$a \sim a_0 + a_1 Pe^{-\beta} \quad \text{and} \quad H'_0(a) \sim \left[-\frac{\rho_0 a_1}{\sigma} \right] Pe^{-\beta}, \tag{5.4}$$

where $\beta = k/(2k - 1)$ and the leading-order contact position is indeed

$$a_0 = 1 - \frac{1}{\rho_0}. \tag{5.5}$$

Note that increasing the rainfall rate, $\rho_0 \rightarrow \infty$, sends $a \rightarrow 1$, and overland water saturates the entire hillslope. In contrast, the limit $\rho_0 \rightarrow 1^+$ reduces the seepage zone size to zero, as anticipated in § 3. The correction factor of a_1 in (5.4) can be calculated as an eigenvalue via the solution of a boundary-value problem (cf. (D9a)). Finally, note that as $Pe^{-1} \rightarrow 0$, the gradient at the transition between overland and groundwater flows, $H'_0(a) \rightarrow 0$.

As we show in § 6.1, in order to find the speed of the seepage zone growth, we need to find the initial depth of the groundwater outside the seepage zone first. We can find this initial depth by solving (5.1a), which can be rearranged as

$$\sigma \frac{dH_0}{dx} = \frac{\rho_0(1 - x)}{H_0(x)} - 1 \quad \text{for } x \in [a_0, 1], \tag{5.6}$$

with a boundary condition $H_0(a_0) = 1$. This first-order nonlinear ordinary differential equation (ODE) does not have an explicit analytical solution; it can either be solved numerically, or we can investigate its shape in different limits.

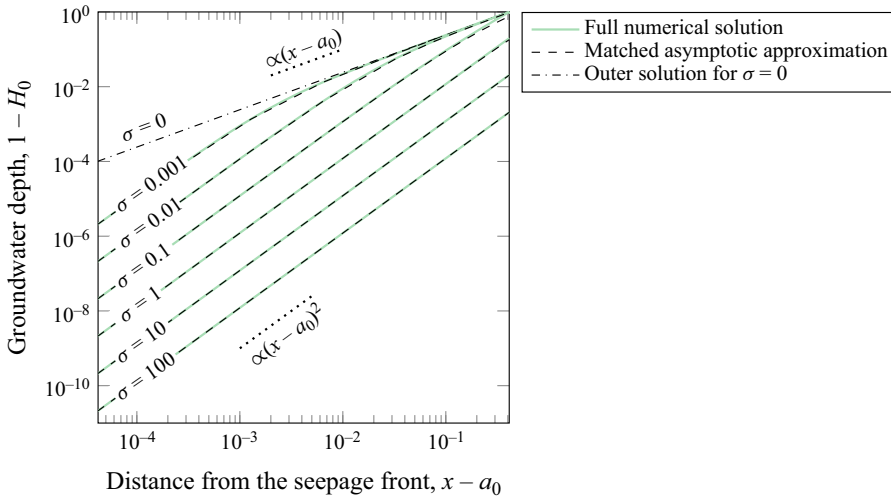


Figure 6. Comparison of groundwater depth given by (5.6) (full numerical solution) with the matched asymptotic approximation given by (5.7).

5.1. Analytical solution as $\sigma \rightarrow 0$

One quite useful limit is to consider $\sigma \rightarrow 0$, corresponding to the infinitely thin porous layer limit. In Appendix E, we derive the outer asymptotic expansion for H_0 in terms of σ , (E2), its inner expansion around $x = 0$ (E4), and finally match them to form the following composite approximation for $H_0(x)$:

$$H_0(x) = \rho_0(1 - x + \sigma - \sigma e^{-(x-a_0)/\sigma}), \quad \text{for } x \in [a_0, 1]. \quad (5.7)$$

As shown in figure 6, this asymptotic solution provides a good approximation of the groundwater shape both for small σ values and, surprisingly, also for large σ values. In the latter case, H_0 becomes a quadratic function,

$$1 - H_0 \sim \frac{\rho_0}{2\sigma}(x - a_0)^2, \quad (5.8)$$

which is also a limiting behaviour of our matched asymptotic solution (5.7) as $x \rightarrow a_0$.

6. Short-time asymptotics

This section relates to the asymptotic limits of $t \rightarrow 0$, $\mu \rightarrow \infty$ and $\rho = \rho_0 r \rightarrow \infty$ in (4.2).

6.1. Groundwater rise and propagation of the seepage zone

Having derived certain analytical properties of the steady-state configuration, $H_0(x; \rho_0)$ (used as an initial condition), we can now study the short-time behaviour of the system as the rain input is set to ρ . As argued at the start of § 4, this is a good approximation, when the rainfall duration is much shorter than the characteristic time of the groundwater transfer to the channel.

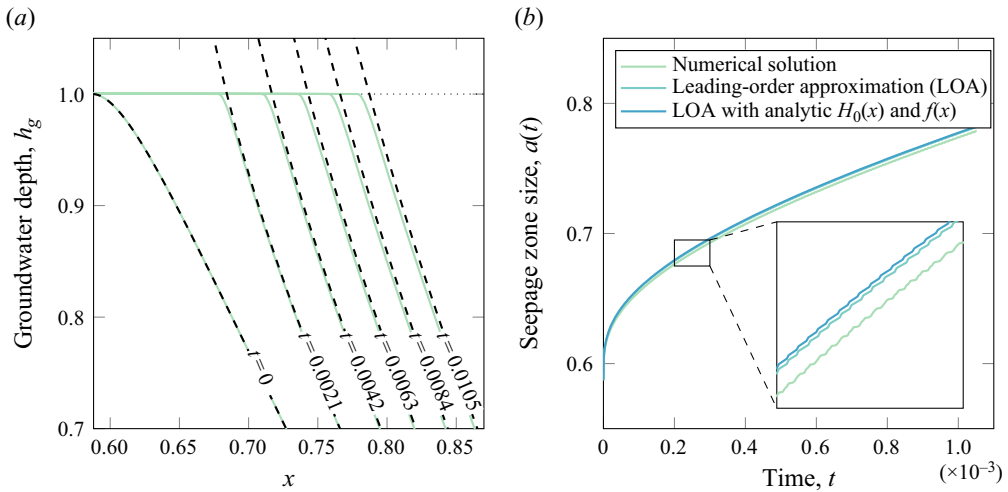


Figure 7. (a) Comparison of the numerical solution of the groundwater shape (solid lines) with the outer solution developed in Appendix F (dashed lines) at different times t . The corresponding size of the seepage zone is presented in (b). A small region is magnified to highlight differences between the presented approximations. The lines are not smooth due to the $h(x)$ interpolation error.

As shown in Appendix F, the outer solution outside the seepage zone (4.3b) can be expanded into a regular series expansion in powers of time t :

$$H_{outer}(x, t) \sim H_0(x; \rho_0) + \left[\frac{\rho - \rho_0}{f(x)} \right] t + O(t^2). \tag{6.1}$$

This approximation assumes that $x - a(t) = O(1)$. The approximation (6.1) thus indicates that the groundwater rises in a fashion proportional to time and the difference between current and prior rain input; it correctly describes the shape of the groundwater except for a thin boundary layer at $x = a(t)$ of thickness of $O(\sqrt{t/(\rho - \rho_0)})$ (see figure 7a). Therefore, for intense rainfall, $\rho \gg 1$, we can neglect the effect of this boundary layer.

We may use the outer groundwater approximation, (6.1), in order to predict the motion of the contact line, $x = a(t)$. Setting $H_{outer} = 1$ gives, in implicit form,

$$t \sim \frac{f(x = a(t))}{\rho - \rho_0} (1 - H_0(x = a(t))) \equiv \mathcal{T}(x = a(t)). \tag{6.2}$$

In order to calculate the above, we must solve two first-order ODEs: (5.6) for the height, $H_0(x)$, and (C2) for the head, $h_g(\hat{z})$, itself used in the calculation of $f(x)$. Alternatively, one can use the analytical approximations for $H_0(x)$ given by (5.7), and $f(x)$ given by (C6) or (C7). Figure 7(b) compares these approximations with the location of the saturation front computed from a full numerical solution of the 1-D model. As we observe based on the difference between the full numerical solution and leading-order approximation (LOA), neglecting the boundary layer around $a(t)$ introduces a small error when estimating the seepage zone size. Replacing the ODEs with analytical approximations for $f(x)$ and $H_0(x)$ in (6.2) also introduces an error, but it is significantly smaller.

6.2. Evolution of the overland flow

Now, knowing how the seepage zone propagates, we can develop a time-dependent solution for the overland flow. Our goal is to extract how the overland flow into the river,

$Q_s(x = 0, t)$, evolves in time, taking into account the effects of increased rainfall and the seepage zone growth.

6.2.1. Problem reduction under $Pe \rightarrow \infty$ limit

The equation for overland flow is given by (4.3a) with the initial condition satisfying steady state (5.1b). We rescale according to

$$\eta = \mu^{1/k}(H - 1) \quad \text{and} \quad T = \mu^{1/k}t. \quad (6.3)$$

Here, $\eta = \eta(x, T)$ is the rescaled surface water height $h_s = H - 1$. Then (4.3a) can be written as

$$\frac{\partial \eta}{\partial T} - k\eta^{k-1} \frac{\partial \eta}{\partial x} - Pe^{-1} \frac{\partial^2 \eta}{\partial x^2} = \rho, \quad (6.4)$$

and (5.1b), which provides the initial condition, H_0 , is

$$1 + \eta^k - Pe^{-1} \frac{d\eta}{dx} = \rho_0(1 - x), \quad (6.5)$$

where, as before, $Pe^{-1} = \sigma/\mu^{1/k}$. Following (4.3a) and (4.3c) the boundaries conditions are

$$\partial_x \eta(0, t) = 0, \quad \eta(a(t), t) = 0. \quad (6.6a,b)$$

Note that the characteristic time it takes the overland flow to reach the channel ($\mu^{-1/k}T_0 \approx 0.1$ day) is much shorter than the characteristic time describing the groundwater flow ($T_0 \approx 1000$ days), and has a similar order of magnitude as a typical rainfall duration. As a result, a short-time approximation is not satisfactory to describe flow variation during a single rainfall event.

The solution for general times can be obtained by considering the $Pe \rightarrow \infty$ limit, similarly as we did when analysing the steady state. This limit allows us to neglect the diffusion term everywhere except for a negligibly thin boundary layer around $x = a$.

In the limit $Pe \rightarrow \infty$, we expand $\eta = \eta_0 + Pe^{-1}\eta_1 + \dots$, and (6.4) becomes a first-order hyperbolic PDE:

$$\frac{\partial \eta_0}{\partial T} - [k\eta_0^{k-1}] \frac{\partial \eta_0}{\partial x} = \rho, \quad x \geq 0. \quad (6.7a)$$

For $0 \leq x \leq a(t)$, there is an initial condition given by

$$\eta_0(x, 0) = \rho_0^{1/k}(a_0 - x)^{1/k}, \quad (6.7b)$$

where we have used the fact shown in Appendix D that $a_0 = 1 - 1/\rho_0$ (cf. (5.5)). The above initial condition is defined along the entire initial seepage zone, $x \in [0, a_0]$. Note that neglecting the diffusion term results in a kinematic wave equation, for which the downstream boundary condition (6.6a) is no longer required.

6.2.2. Implicit solution using methods of characteristics

The system (6.7) can be solved using the method of characteristics (Lagrange–Charpit equations). The solution is given by characteristic curves (T, x, η_0) , now parameterised by

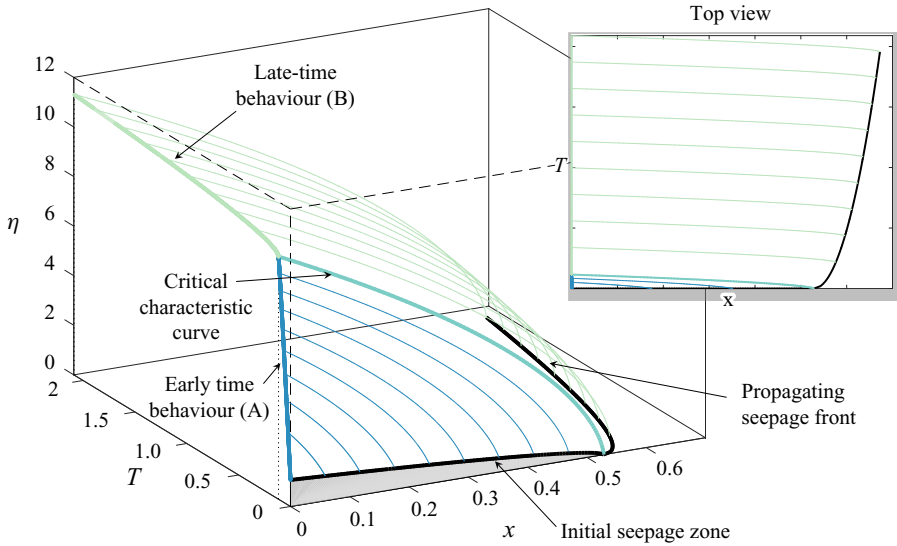


Figure 8. Characteristic curves given by (6.9) for parameters listed in table 1. Dark blue lines represent curves originating from the initial seepage zone, and light green lines represent curves originating from the propagating front of the seepage zone.

(s, τ) , where τ is the characteristic curve parameter, and s parameterises the initial data. The characteristic equations are

$$\frac{dT}{d\tau} = 1, \quad \frac{dx}{d\tau} = -k\eta_0^{k-1}, \quad \frac{d\eta_0}{d\tau} = \rho. \tag{6.8a}$$

The initial conditions are specified along $\tau = 0$ according to two types of characteristics. One set of characteristics emerges from $T = 0$, at the location of the initial water shape, $H_0(x)$, valid for $x \in [0, a(t)]$. Another set of characteristics emerges from the propagating front, $x = a(t)$, representing the groundwater reaching the surface and, hence, initiating surface flow.

Parameterising the initial data by $x = s$, we have

$$(T(s, 0), x(s, 0), \eta_0(s, 0)) = \begin{cases} (0, s, H_0(s)), & s \in [0, a(t)], \\ (\mu^{1/k}T(s), s, 0), & s \in [a(t), \infty). \end{cases} \tag{6.8b}$$

The first condition will use the initial surface height, $H_0(s) = \rho_0^{1/k}(a_0 - s)^{1/k}$ given by (6.7b). The second condition is essentially specified along the moving front, $(T, x, \eta_0) = (T, a(t), 1)$, but we have written it in terms of the s -independent variable, and the rescaled function T in (6.2). In summary, the characteristic solution can be obtained via direct integration of (6.8), giving

$$\left. \begin{aligned} T(s, \tau) &= T(s, 0) + \tau, \\ x(s, \tau) &= x(s, 0) - \rho^{-1}[\eta_0(s, 0) + \rho\tau]^k + \rho^{-1}[\eta_0(s, 0)]^k, \\ \eta_0(s, \tau) &= \eta_0(s, 0) + \rho\tau. \end{aligned} \right\} \tag{6.9}$$

We show an example of the characteristics and characteristic projections in figure 8.

Once the solution is determined, a key quantity of interest is the surface water height at $x = 0$, as it determines the overland flow reaching the river. We denote this critical point

along the characteristics as $(T, \eta_0) = (T^*, \eta^*)$. By setting $x(s, \tau) = 0$ in the characteristic equations (6.9) and eliminating τ from the second equation, we obtain

$$\begin{pmatrix} T^* \\ \eta^* \end{pmatrix} = \begin{pmatrix} T(s, 0) + \frac{1}{\rho}(\eta^* - \eta_0(s, 0)) \\ (\rho x(s, 0) + (\eta_0(s, 0))^k)^{1/k} \end{pmatrix}. \quad (6.10)$$

We need to consider two cases separately: characteristics starting from the initial seepage zone and characteristics emerging from the propagating seepage front. Each case is given by the different initial conditions, as specified in (6.8b).

In the first case, by substituting the first initial condition from (6.8b) into (6.10), we obtain

$$\begin{pmatrix} T^* \\ \eta^* \end{pmatrix} = \begin{pmatrix} \frac{1}{\rho}(\eta^* - \rho_0^{1/k}(a-s)^{1/k}) \\ (\rho s + \rho_0(a-s))^{1/k} \end{pmatrix}. \quad (6.11)$$

By finding s from (6.12a) and substituting into (6.12b) we can express T^* as a function of η^* :

$$T^*(\eta^*) = \frac{1}{\rho} \left[\eta^* - \left(\frac{\rho_0}{\rho - \rho_0} \right)^{1/k} (\rho a_0 - (\eta^*)^k)^{1/k} \right]. \quad (6.12)$$

This equation is satisfied for $\eta^* \in [(\rho_0 a_0)^{1/k}, (\rho a_0)^{1/k}]$. The lower limit corresponds to the initial height, and the upper limit corresponds to the height reached by the characteristic curve starting at $x_0 = a_0$. At the upper limit, the characteristic curve reaches the river ($x = 0$) at what we refer to as the *critical time*:

$$T_{crit} = \frac{1}{\rho} (\rho a_0)^{1/k}. \quad (6.13)$$

This critical saturation event is associated with the critical characteristic curve highlighted in figure 8.

For those characteristics starting from the propagating seepage front, $x = a(t)$, we substitute the second initial condition from (6.8b) into (6.10):

$$\begin{pmatrix} T^* \\ \eta^* \end{pmatrix} = \begin{pmatrix} \mu^{1/k} \mathcal{T}(s) + \frac{1}{\rho} \eta^* \\ (\rho s)^{1/k} \end{pmatrix}. \quad (6.14)$$

By eliminating s , we can express T^* as a function of η^* :

$$T^*(\eta^*) = \mu^{1/k} \mathcal{T} \left(\frac{1}{\rho} (\eta^*)^k \right) + \frac{1}{\rho} \eta^*. \quad (6.15)$$

By combining (6.12) and (6.15), we can find the height of the surface water, at the river, $x = 0$, value for all times $T \geq 0$. This is done by solving the implicit equation:

$$T^*(\eta^*) = \begin{cases} \frac{\eta^*}{\rho} - \frac{1}{\rho} \left(\frac{\rho_0}{\rho - \rho_0} \right)^{1/k} (\rho a_0 - (\eta^*)^k)^{1/k}, & \text{for } \eta^* \leq (\rho a_0)^{1/k}, \\ \frac{\eta^*}{\rho} + \mu^{1/k} \mathcal{T} \left(\frac{1}{\rho} (\eta^*)^k \right), & \text{for } \eta^* > (\rho a_0)^{1/k}. \end{cases} \quad (6.16)$$

Alternatively, we can express the height of the surface water η^* in terms of the overland component of river inflow, which is represented by the last term in (2.9), $Q_s^* = (\eta^*)^k$.

This leads to the equation:

$$t^*(Q_s^*) = \begin{cases} \frac{1}{\rho}(Q_s^*)^{1/k} - \frac{1}{\rho} \left(\frac{\rho_0}{\rho - \rho_0} \right)^{1/k} (\rho a_0 - Q_s^*)^{1/k}, & \text{for } Q_s^* \leq \rho a_0, \\ \frac{1}{\rho}(Q_s^*)^{1/k} + \mu^{1/k} \mathcal{T} \left(\frac{Q_s^*}{\rho} \right), & \text{for } Q_s^* > \rho a_0. \end{cases} \quad (6.17)$$

Equation (6.17) represents one of the major results of this work, since it provides an implicit expression for the shape of the hydrograph $Q_s^*(t^*)$.

6.2.3. Approximating the hydrograph in an explicit form

We can obtain an approximated explicit form for the $Q_s^*(t)$ function for $Q_s^* > \rho a_0$. In the limit $\mu \rightarrow \infty$ (equivalent to $Pe \rightarrow \infty$), we may expand around the value of Q_s^* at t_{crit} in (6.13), and write

$$Q_s^*(t^*) \sim \rho a (\mu^{-1/k} (t^* - t_{crit})) \quad \text{for } t^* \geq t_{crit}, \quad (6.18a)$$

where we have used $a(t) = \mathcal{T}^{-1}(t)$ from (6.2) to describe the propagation of the wetting front in time. Following approximation (5.7) and (C7), it can be written explicitly as

$$a(t) = \underbrace{a_0}_{term1} + \underbrace{s(t)}_{term2} + \underbrace{\sigma [1 + W_0(-e^{-1-s(t)/\sigma})]}_{term3}, \quad (6.18b)$$

where

$$s(t) = At^{1/(n+1)} \quad \text{with } A = \frac{1}{\rho_0} \left[\frac{n+1}{m} \frac{\rho - \rho_0}{\theta_s - \theta_r} \left(1 - \frac{r_0}{K_s} \right)^{-n} \alpha^{-n} \right]^{1/(n+1)}. \quad (6.18c)$$

Here, $W_0(\cdot)$ is the Lambert W function, and α , θ_s , θ_r , n and m are soil properties used in the Mualem–van Genuchten model (see § C.2).

The first term in (6.18b) corresponds to the flow over the initial seepage zone. The second and third terms represents the growth of flow after reaching the critical point. The third term, in the case of $\sigma \ll 1$, quickly grows from 0 asymptotically reaching σ as $t \rightarrow \infty$, whereas the second term is responsible for further growth of the river flow. Therefore, for thin hillslopes ($\sigma \ll 1$), the growth of river flow after passing the critical point scales proportionally to the ρA factor.

In the next section, we summarise all approximations derived in this section, and validate them by comparing with each other and full numerical solutions of 1-D and 2-D benchmark models.

7. A numerical comparison between different approximations

7.1. Numerical set-up

In Part 2 (Morawiecki & Trinh 2024b), we performed a numerical verification of the assumption of reducing the 3-D benchmark model to a 2-D model. We also conducted a detailed sensitivity analysis, highlighting the dependencies of model parameters on the resultant peak flows. Here, we continue this analysis by comparing the hydrographs and peak flows between the five different approximations derived and discussed in this paper. The approximations are summarised in table 2 in order from the most complex to the simplest.

Approximation	Equations/notes
2-D surface–subsurface model	Richards/Saint Venant equations along a 2-D hillslope, as discussed in Part 2 of this paper.
1-D surface–subsurface model	The 1-D Boussinesq system (2.8), which assumes a thin porous layer limit, $L_z \ll L_x$.
Characteristics (numerically implicit)	Solution given by (6.17), where the $H_0(x)$ and $f(x)$ functions are found numerically using 1-D ODEs (5.6) and (C2). Assumes scenario $\rho_0 > 1$, early time $t \ll 1$, intense rainfall $\rho \gg 1$ and $Pe \gg 1$.
Characteristics (analytically implicit)	Solution given by (6.17), where the functions $H_0(x)$ and $f(x)$ are approximated as (5.7) and (C6). In addition, it assumes that $\sigma \gg 1$, $H_0 \ll 1$.
Characteristics (analytically explicit)	Solution given by (6.18), $t_{crit} < t \ll 1$ (in addition to the assumptions listed before).
Critical flow	Flow estimated as $Q_{crit} = \rho a_0 + \rho_0(1 - a_0)$, equal to the river inflow reached at $t = t_{crit}$ (further discussion in § 8).

Table 2. Summary of the approximations developed in this work.

Parameter	Default value	Parameter range	Parameter	Value
K_s (m s ⁻¹)	1×10^{-5}	$10^{-6} - 10^{-4}$	L_y (m)	18 000
L_x (m)	6.16×10^2	$10^2 - 10^3$	w (m)	5
L_z (m)	6.84×10^2	$10^1 - 10^3$	h_{out} (m)	0.3
S_x (-)	7.5×10^{-2}	$10^{-2} - 10^{-1}$	θ_s (-)	0.488
r (m s ⁻¹)	2.36×10^{-7}	$3 \times 10^{-8} - 3 \times 10^{-6}$	θ_r (-)	0
r_0 (m s ⁻¹)	2.95×10^{-8}	$10^{-9} - 10^{-7}$	n (-)	1.19
n_s (m s ^{-1/3})	5.1×10^{-2}	$10^{-2} - 10^{-1}$		

Table 3. Default values and ranges of parameters used to perform the sensitivity analysis. The part on the right presents parameters not varied during the sensitivity analysis.

Similar to the methodology presented in Parts 1 and 2, we assess the performance of the above models in two ways. First, we compare the hydrograph obtained using each model for standard values of parameters characterising UK catchments, as listed in table 3. Second, we run a sensitivity analysis by varying seven model parameters, one at a time, while keeping the others at their default values, and measuring the peak flow in the river after an intensive rainfall. In both numerical experiments, we consider a uniform rainfall over a duration of 24 h.

7.2. Comparing the hydrographs

A comparison of the hydrographs obtained under the different approximations is presented in figure 9. First, we note that the 1-D models formulated in this paper produce similar hydrographs to the 2-D model from the previous part of our work. However, the 1-D models slightly underestimate the flow, and the solutions are not smooth around the critical point separating early-time and last-time growth.

Second, all approximated solutions of the 1-D model produce consistent results for $t \leq t_{crit}$ (except for the explicit solution, which is valid only for $t > t_{crit}$). The results are also similar for $t > t_{crit}$, but inaccuracies related to different approximations start

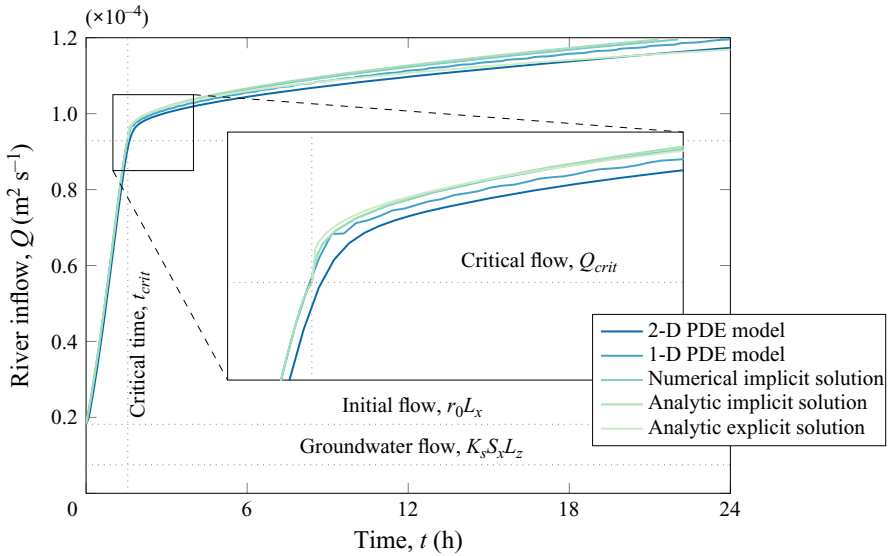


Figure 9. Hydrograph computed using approximations listed in table 2 for default values of parameters given in table 3. The graph area around the critical point is magnified. Numerical instabilities are observed for the 1-D model, caused by the finite discretisation of space, which does not allow capturing the exact location of the seepage, and by instabilities related to the governing equation for the seepage zone (2.8a), characterised by a very small diffusive term.

to become noticeable. For example, the implicit solution closely follows the 1-D model solution, but with the flow slightly shifted towards the higher values. This deviation is caused by neglecting the boundary layer characterising the groundwater shape around the critical point. As discussed in Appendix F, this inaccuracy decreases as ρ increases. Replacing numerical solutions for $f(x)$ and $H_0(x)$ with their analytical approximations seems to have a negligible effect on the model for typical sizes of catchment parameters.

Similarly, using approximation (6.18) for the explicit solution leads to the underestimation of the groundwater rise rate, which slows down the growth of flow for higher t values. In addition, the flow around $t = t_{crit}$ is slightly overestimated as a result of neglecting the variation of the $(Q_s^*)^{1/k}$ term appearing in the implicit solution (6.17). Despite these small inaccuracies, the explicit solution still seems to produce excellent qualitative and quantitative agreement. Moreover, due to its simple form, the explicit form allows us to directly understand the effect of various catchment properties on the expected peak flows.

7.3. Sensitivity analysis

We chose seven physical parameters for the sensitivity analysis: catchment width L_x , aquifer depth L_z , elevation gradient along the hillslope S_x , hydraulic conductivity K_s , precipitation rates r and r_0 and Manning’s constant n_s . We varied each parameter within the range of its typical values presented in table 3, while keeping the other parameters constant. In each case, we simulated the model’s response to a 24-hour-long rainfall event (as shown in figure 9), and then measured the peak river inflow $Q(x = 0, t)$ reached at the end of this period. The results of the sensitivity analysis are presented in figure 10.

We note that the dimensionless parameter determining the existence of the initial seepage zone is given by $\rho_0 = rL_x / (K_s L_z S_x)$. Therefore, as the dimensional parameters

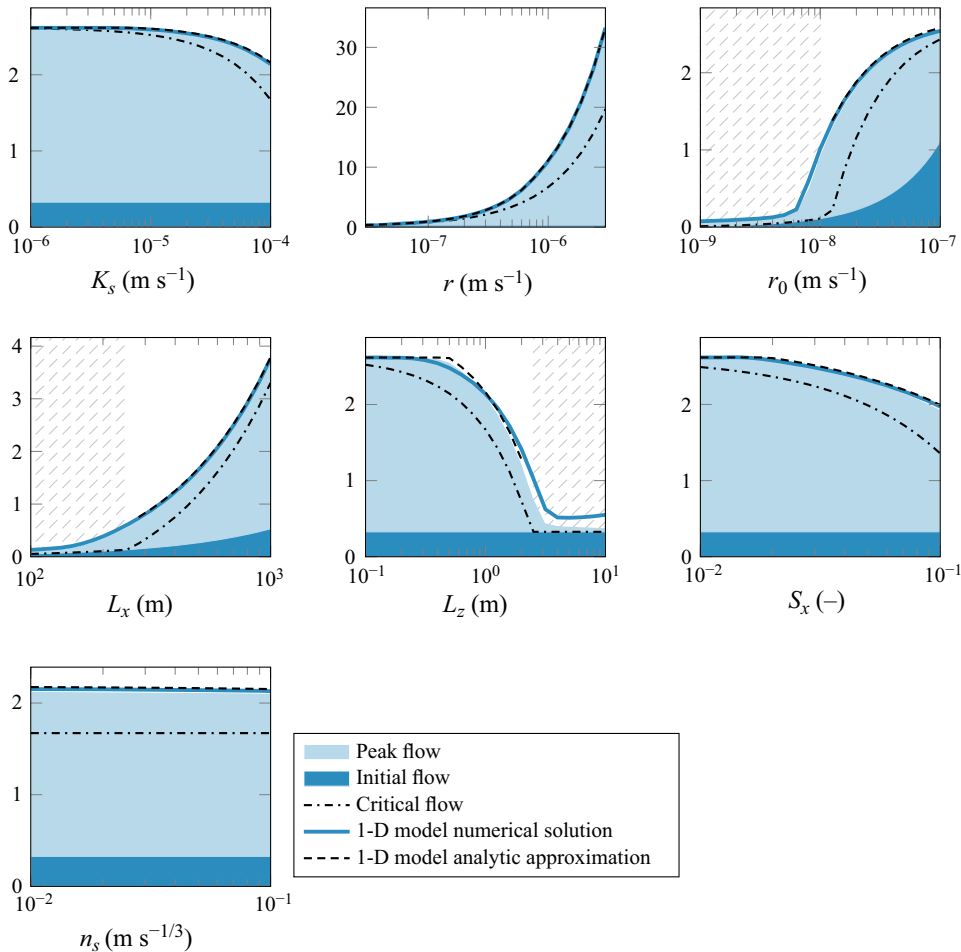


Figure 10. Sensitivity analysis results showing the dependence between the peak flow reached after 24 h of intensive rainfall and seven different model parameters. The predictions conducted using four models of varying complexity are presented. The dashed region represents the parameter range, for which there is no initial seepage zone ($\rho_0 < 1$).

are varied, the initial condition may not involve an initial seepage zone if $\rho_0 < 1$. The parameter ranges for which that happens are marked by a dashed region in [figure 10](#). We observe that as long as there is an initial seepage zone, the analytical approximations of the hydrograph are largely accurate over the range of tested parameters.

As expected, the (total) peak flows reached are higher than the maximum levels set by the critical saturation flow, given by (8.2), since the latter only describes the flow reached during the early-time phase. Nevertheless, for most parameter values, the critical flow curve provides a good approximation of the peak flows. In Part 2 of our work, based purely on the 3-D and 2-D simulations, we arrived at the same conclusion.

The cases where the critical flow value highly underestimates the peak flow are around $\rho_0 = 1$. In these cases, either the seepage zone does not initially exist but the soil is almost fully saturated near the river (ρ_0 slightly lower than 1), or it exists but is very small (ρ_0 slightly larger). In both cases, rainfall causes the seepage zone to grow significantly relative

to its initial size; however, this growth is not captured by the time-independent estimate (8.2).

8. Summary of the key hydrograph features

In figure 9 in the previous section, we showed a typical shape of a hydrograph given by the 1-D model. Here, we summarise the main features of the hydrograph and its importance in benchmarking.

As discussed before, two different phases are visible: phase 1, an early-time fast rise caused by water accumulating over an initial seepage zone; and Phase 2, a late-time slow rise caused by a growing seepage zone. The analytical approximation presented in § 6.2.3 shows that the growth of the overland flow in the second phase can be approximated as $Q_s(t) \approx \rho a(t)$, i.e. it corresponds to the total precipitation rate over the seepage zone $a(t)$ slowly growing in time t . Together with the groundwater flow $Q_g = 1$, they give a total river inflow $Q(t) = 1 + \rho a(t)$, which in dimensional units is

$$Q(t) = K_s S_x L_z + r L_x a(t) = r_0 L_x (1 - a_0) + r L_x a(t), \tag{8.1}$$

where $a_0 = 1 - K_s S_x L_z / r L_x$ is the size of the initial seepage zone.

Following § 6.2, the transition from the first to the second phase corresponds to the moment when the characteristic curve starting from the furthestmost point of the initial seepage zone reaches the river ($x = 0$). This observation allowed us to estimate the dimensionless critical flow, which in dimensional units correspond to (8.1) with $a(t) = a_0$:

$$Q_{crit} = \underbrace{K_s S_x L_z}_{\text{groundwater flow}} + r L_x \underbrace{\left(1 - \frac{K_s S_x L_z}{r_0 L_x}\right)}_{\text{overland flow}}. \tag{8.2}$$

It is reached at the critical time t_{crit} given by (6.13), which in dimensional units is

$$t_{crit} = \frac{L_z}{r} \left[\frac{S_x^{1/2} K_s n}{L_z^{k-1}} \left(\frac{L_x r}{K_s S_x L_z} - \frac{r}{r_0} \right) \right]^{1/k}. \tag{8.3}$$

Following the above event, further growth (8.1) is slow, which is a result of the difference of $\mu^{1/k} \approx 10^4$ factor between the characteristic timescale of overland flow (responsible for Phase 1) and groundwater flow (responsible for Phase 2). Therefore, Q_{crit} may be a good approximation of the flow even long after the critical time.

We highlight a few additional features of our 1-D benchmark model.

- (i) When the groundwater component of Q_{crit} (8.2) is much smaller than the overland component (e.g. during intensive rainfalls), the critical flow reached during extreme rainfalls can be approximated by

$$Q_{crit} \approx r L_x \left(1 - \frac{K_s S_x L_z}{r_0 L_x}\right). \tag{8.4}$$

Since the consecutive river flow rise is slow, the above estimate can be used as an approximation of the peak flow reached, assuming that the rainfall is long enough to reach the critical time, t_{crit} .

- (ii) Under this approximation, the critical point can be represented as a function of three parameters: rainfall intensity, catchment area (since the flow scales proportionally to both the hillslope width L_x and catchment length L_y), and the $K_s S_x L_z / (r_0 L_x)$ factor,

which is equal to the fraction of groundwater flow $K_S S_X L_z$ to the mean total flow $r_0 L_x$. This last parameter can be related to what is often referred to as the BFI (Gustard, Bullock & Dixon 1992, Section 3.1.2).

- (iii) There are some similarities between this expression and other models used in hydrology. Equation (8.4) is a special case of the so-called rational method, which assumes that river flow is proportional to area and precipitation rate (see Bedient *et al.* 2008, chapter 1.5). The proportionality constant (runoff coefficient) here is identified as $1 - \text{BFI}$.

The BFI appears in many statistical methods used in flood estimation, which, unlike our physically-based approach, are based on applying statistical methods such as linear regression to the available catchment data. A notable example is the Flood Estimation Handbook (FEH) flood estimation method by Kjeldsen *et al.* (2008). It assumes that the median of the annual maximum flow (QMED) scales as $\text{QMED} \propto 0.0460^{\text{BFIHOST}^2}$, where BFIHOST is a soil-based BFI estimator. Note that, similarly to (8.4), the predicted flow decreases with the BFI, but in a nonlinear fashion. Interestingly, other catchment descriptors used in the FEH method include the catchment's area and precipitation, which, like BFI, are also related to the maximum annual flow through nonlinear functions, selected to fit the available data.

Even though our 1-D benchmark model is based on a series of simplifying assumptions (e.g. a thin porous layer and pre-existing seepage zone), which are often not satisfied in real-world catchments, its predictions seem to be reasonable in comparison with data-based catchment models. The connection between our simple scaling laws, shown above and derived analytically from a physical model, and statistical models such as the aforementioned FEH method, which are formulated in a completely different fashion, is intriguing. These results will be presented in a forthcoming work by the present authors, and can also be found in Morawiecki (2023).

9. Conclusions

The primary aim of our work has been to develop and analyse a rigorous benchmark scenario for coupled surface–subsurface flows in a typical catchment. We have achieved this goal by first characterising the typical parameter scales according to the available data on UK catchments (Part 1), formulating and computing the 3-D model and its reduction (Part 2) and finally applying methods in asymptotic analysis to a reduced model valid for catchments dominated by overland dynamics (Part 3).

In this last work, our analysis yields valuable scaling laws for the peak flows (see § 8), which precisely quantify the separation of timescales observed in the hydrographs following an intense period of rain (see a distinct early- and late-time behaviour in figure 9). In particular, we find that the early-time behaviour is governed by rainfall accumulation over a pre-existing seepage zone, followed by a slower flow rise in late time. This latter stage is limited by the speed with which the rising groundwater increases the size of the seepage zone.

All approximations are in good agreement with hydrographs produced by the more complete 1-D and 2-D models, and allow accurate prediction of river peak flows over a wide range of catchment parameters (as long as the underlying assumptions are satisfied). However, different regimes not captured by our model could be studied, including for example behaviour of catchments with no initial seepage ($\rho_0 < 1$), and late-time catchment behaviour in case of long continuous rainfalls ($t = O(1)$).

10. Discussion

Our investigations in these three parts have been limited to fairly elementary scenarios and geometries. However, our final results involving the derivation of analytical/asymptotic scaling laws with a clear underlying structure may serve as a valuable benchmark for other hillslope or catchment models. Currently, we observed that the benchmarking of coupled surface–subsurface catchment models has been limited to quantitative numerical comparisons, either with real-world observations or with the numerical output of other schemes (e.g. Maxwell *et al.* 2014). Although such studies allow practitioners to evaluate the given model's performance in specific conditions, they do not necessarily allow one to draw general conclusions about each model's limit of applicability. As a result, we have no guarantee that a given model will still perform well if applied in situations not captured in the training or validation data as demonstrated in many studies (e.g. Klemeš 1986; Beven 2019).

10.1. *Applications of the benchmark to model intercomparisons*

Deriving asymptotic estimates for the hydrograph, as done in this work, opens another possibility: models can be compared at a more fundamental level. For instance, we can check if the flows produced by various models scale with the different catchment properties in the expected fashion (and under the conditions we have specified). Detecting situations or limits where the predictions diverge can allow us to better understand the limitations of different models and shed light on how these models can be extended beyond their current limit of applicability. This idea is explored in our two forthcoming works (Morawiecki & Trinh 2023*a,b*).

As a particular example, statistical models used for flood estimation (such as the FEH method, briefly discussed at the end of § 8) require the selection of empirical catchment descriptors for use in regression formulae to predict flood response (Kjeldsen *et al.* 2008). In a forthcoming paper (Morawiecki & Trinh 2023*b,c*), we show that the expression (8.4) can be used to derive a simple expression for predicting peak monthly and annual river flows. This prediction turns out to be highly accurate when applied to real-world data. We then use this result to discuss the limitations of the existing statistical model from the FEH.

Similarly, we can compare the analytical solutions developed within the physical benchmark model with the flow hydrographs generated via conceptual rainfall-runoff models (see the model overview by Peel & McMahon 2020). Although these models use continuous-time rainfall data to generate hydrographs, they are typically not based on the same fluid dynamical models of surface and subsurface flows. Consequently, they can be characterised by different scaling laws than the ones found in this paper. In our forthcoming work (Morawiecki & Trinh 2023*a*), we demonstrate this discrepancy by studying two models. The first is a probability-distributed model (PDM) used by, e.g. the Environment Agency National Flood Forecasting System (Moore 2007). The second is the grid-to-grid model by Bell *et al.* (2007), used by the UK Centre for Ecology and Hydrology to provide real-time flow predictions in the UK. In both cases, our simple benchmark scenario allows the identification of key differences between physical and aforementioned conceptual models.

10.2. *Extensions and generalisations of the benchmark scenario*

Another important line of inquiry is the generalisation of the analysis we have presented to situations that are more representative. Such extensions can involve the analysis of non-uniform rainfall, varying initial conditions to study the response to extended periods

of drought, or catchments response to sudden drawdown or outlet water level. These asymptotic regimes have already been studied using the Boussinesq approximation (see, e.g. Parlange *et al.* 2001; Mizumura 2002). However, our coupled surface–subsurface approach could allow us to better understand the potential role of the seepage dynamics. Then, analytical approximations of the drying process could be used to assess the assumptions of the conceptual rainfall-runoff models, especially since dry periods are sometimes used for a preliminary parameter calibration (Lamb 1999). Finally, we highlight the importance of multiporosity regions in hydrological modelling; these lead to effects such as a preferential flow (Beven & Germann 2013). We provide further details on potential extensions of this study in Morawiecki (2023, chapter 9).

Lastly, it would be interesting to obtain experimental validation of the studied regimes. There have been quite a few lab- and field-scale experimental studies, in which a constant rainfall was artificially generated. However, many of them (e.g. Pauwels & Uijlenhoet 2018) focus on systems limited to the groundwater flow only. There are some experimental studies in which rainfall we observed to yield seepage growth, e.g. Abdul & Gillham (1989), Kollet *et al.* (2017) and Scudeler *et al.* (2017). However, in these experiments, the soil was initially dry, i.e. there was no initial seepage, so they correspond only to the $\rho_0 = 0$ case. It would be interesting to conduct controlled experiments with more realistic settings, i.e. with an already developed groundwater table, and compare the resultant hydrograph with our model predictions.

Acknowledgements. We thank Sean Longfield (Environmental Agency) for many useful interactions and for motivating this work via the 7th Integrative Think Tank hosted by the Statistical and Applied Mathematics CDT at Bath (SAMBa). We also thank Thomas Kjeldsen (Bath), Tristan Pryer (Bath) and Rob Lamb (Lancaster/JBA Trust) for insightful discussions. We are indebted to the reviewers and the JFM editorial team for their comments and suggestions that were instrumental in the final development of this paper.

Funding. P.M. is supported by a scholarship from the EPSRC Centre for Doctoral Training in Statistical Applied Mathematics at Bath (SAMBa), under the project EP/S022945/1.

Declaration of interests. The authors report no conflict of interest.

Author ORCIDs.

 Piotr Morawiecki <https://orcid.org/0000-0002-7136-7980>;

 Philippe H. Trinh <https://orcid.org/0000-0003-3227-1844>.

Appendix A. List of symbols

For ease of reference, we provide a list of symbols in [table 4](#).

Appendix B. Relation between the 1-D Boussinesq equation and the 2-D Richards equation

In this appendix, we provide additional details on the derivation of the 1-D model presented in this paper, in connection with the physical models presented in Part 2. We shall explain how the governing equations (2.3) and (2.5) relate to the 2-D Richards equation given in (5.9a) from Part 2 (Morawiecki & Trinh 2024b). Some parts of the following are classical, and relate to the derivation of the Boussinesq equation (cf. Bear & Verruijt 1987 for details); our new contribution is to consider the influence of the overland flow in the seepage zone on the Boussinesq equation and to couple this latter equation with its standard formulation for the remaining part of the domain.

In this study, we assume that hillslope flow is predominantly 2-D in the xz cross-section; this reduction from three dimensions to two dimensions is discussed in detail in Part 2.

Group	Symbol	Description
Coordinates	x	Spatial coordinate along the hillslope
	t	Time
Variables	H_g	Groundwater depth
	h_s	Surface water depth
	H	Total depth ($H_g + h_s$)
	H_0	Initial value of total depth
	Q_g	Groundwater flux
	Q_s	Overland flux
Catchment properties	L_z	Thickness of the porous layer
	S_x	Slope along the hillslope
	r	Rainfall intensity
	K_s	Hydraulic conductivity
	f	Mean drainable porosity (typically a function of x)
	θ_s, θ_r	Saturated and residual water content
	α, n, m	Mualem–van Genuchten model parameters
	T_0	Characteristic timescale of groundwater flow
	n_s	Manning roughness coefficient
	k	Exponent form the Manning’s law (typically $k = 5/3$)
	Dimensionless constants	σ
μ		Overland to groundwater flux ratio
ρ		Precipitation rate to groundwater flux ratio
ρ_0		Mean precipitation rate to groundwater flux ratio
$\Delta\rho$		Difference between ρ and ρ_0
Pe		Péclet number for the overland flow
a		Saturated fraction of the hillslope
a_0		Leading-order approximation of a for $Pe \rightarrow \infty$
Characteristic curves		T
	η	Rescaled surface water height for the overland flow model
	τ	Characteristic curve parameter
	s	Parameter describing initial data
	T^*, η^*, Q_s^*	Value of time, surface water height and surface flow, when the characteristic curve reaches $x = 0$
	t_{crit}	Critical time
	Q_{crit}	Critical flow
Simulation parameters	N_x	Spatial mesh resolution
	N_t	Number of time steps

Table 4. List of symbols

In addition, we consider the small aspect ratio limit, $L_z \ll L_x$ and, hence, $\beta_{zx} = L_z/L_x \rightarrow 0$. In the groundwater region, following (5.9a) from Part 2, the leading-order flow then satisfies

$$\frac{d\theta}{dh} \Big|_{h=h'_g} \frac{\partial h'_g}{\partial t} = \frac{\partial}{\partial \hat{z}} \left[K_r(h'_g) \left(\frac{\partial h'_g}{\partial \hat{z}} + 1 \right) \right], \quad 0 < \hat{z} < 1, \quad (\text{B1})$$

with $\hat{z} = 0$ corresponding to the bottom of the aquifer and $\hat{z} = 1$ corresponding to the top surface. Note that for $\hat{z} < H$, the Richards equation becomes much simpler, since for saturated soil we have $d\theta/dh = 0$ and $K_r(h) = 1$. Solving (B1) and imposing the no-flow

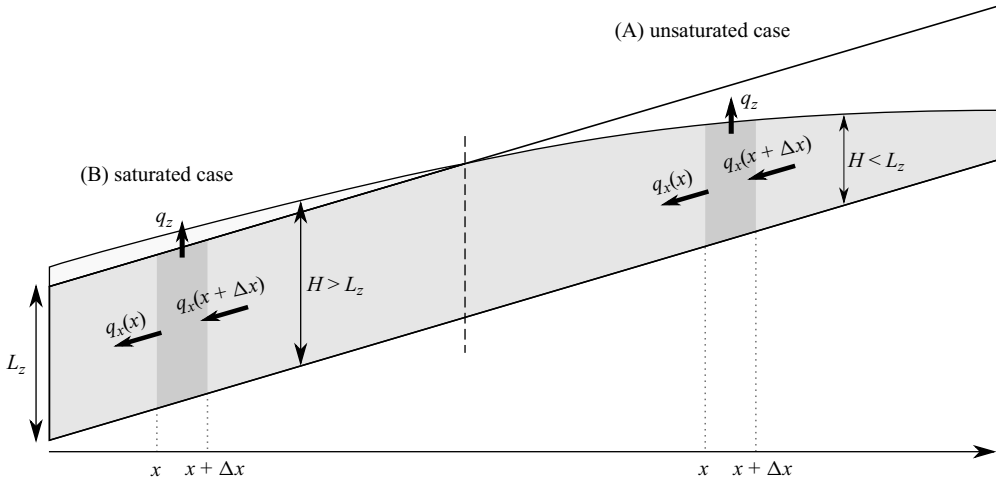


Figure 11. Control volume (A) outside the seepage zone and (B) inside the seepage zone. One-way arrows represent flow in and out of the control volumes.

boundary condition at the bottom of the aquifer $\hat{z} = 0$, we obtain

$$h'_g(\hat{x}, \hat{z}, t) = H'(\hat{x}, t) - \hat{z}, \quad 0 < \hat{z} < H'(\hat{x}, t), \quad (\text{B2})$$

which corresponds to a hydrostatic vertical profile of pressure. Note that based on the above solution, for regions of completely saturated soil, the 2-D function $h'_g(\hat{x}, \hat{z}, t)$ can be replaced by the 1-D indicator, $H'(\hat{x}, t)$. The curve $\hat{z} = H'(\hat{x}, t) \in (0, 1]$ corresponds to the groundwater table, which separates between saturated (where $h'_g > 0$) and unsaturated (where $h'_g < 0$) regions, if both coexist.

We assume that the system is configured as shown in figure 11. Thus, it is divided into a region B (fully saturated case), where $0 \leq \hat{x} \leq a(t)$ and the ground is entirely saturated, with $H = 1$. Similarly, we have region A (unsaturated case) for $\hat{x} > a(t)$, where $H < 1$ and there is an unsaturated column where $H < \hat{z} < 1$.

For ease of interpretation, we shall return, for the next few subsections, to dimensional quantities (related to the governing equation (2.7)). In addition, it is more convenient to use Richards equation expressed in the Cartesian coordinates (x, z) . In this coordinate system, (B2) becomes

$$h_g(x, z, t) = S_x x + H(x, t) - z, \quad \text{for } x \in [0, L_x], \quad z \in [0, L_z], \quad (\text{B3})$$

where $L_z \hat{z} = z - S_x x$, $H = L_z H'$ and $h_g = L_z h'_g$. Following Darcy's law, we have $\mathbf{q} = K_s \nabla (h_g + z)$. After substituting (B3), we obtain the leading term of horizontal flow:

$$q_x = -K_s \frac{\partial}{\partial x} (h_g + z) = -K_s \left(S_x + \frac{\partial H}{\partial x} \right). \quad (\text{B4})$$

Note that the above point flux is independent of z . Multiplying by H , we thus see that the total (unsigned) flow along the hillslope is then given by

$$Q_g = H |q_x| = K_s H \frac{\partial H}{\partial x} + K_s H S_x. \quad (\text{B5})$$

Next, we consider the unsaturated part of the hillslope (region A) and the seepage zone (region B) separately since the latter requires adding an overland flow component.

B.1. Region A: governing equation outside the seepage zone, $H < 1$

Let us consider region A, where there is a layer of unsaturated soil. Recall that the pressure h_g is zero at the free surface of the groundwater, where $z = S_x x + H_g(x, t)$. This allows us to set the integration constant H appearing in (B3) to $H(x, t) = H_g(x, t)$.

We consider the control volume, V , within the column horizontally bounded by $[x, x + \Delta x]$, as shown in figure 11. By conservation and the divergence theorem, it is argued that the total flux integral around the boundary, ∂V , is zero and, hence,

$$0 = \oint_{\partial V} \nabla(h + z) \cdot \mathbf{n} \, dl$$

$$= -H(x)q_x(x) + H(x + \Delta x)q_x(x + \Delta x) + \int_x^{x+\Delta x} q_z \Big|_{z=S_x x + H(x)} \, dx. \quad (B6)$$

Richards equation in the fully saturated groundwater region reduces to $\nabla \cdot \mathbf{q} = K_s \nabla^2(h + z) = 0$ (as discussed following (B1)). Thus, in the $\Delta x \rightarrow 0$ limit, we can approximate the vertical flux at the top of the saturated zone as

$$q_z^{top} = q_z|_{z=S_x x + H(x)} = -\frac{\partial}{\partial x}(Hq_x) = K_s \frac{\partial}{\partial x} \left(HS_x + H \frac{\partial H}{\partial x} \right), \quad (B7)$$

where we have used the expression for q_x derived in (B4).

Now, let us consider the unsaturated zone above the groundwater table (dashed region in figure 11). The inflow from the top boundary is $r(t)$, and the outflow to groundwater is q_z^{top} . If during a rainfall the inflow is greater than the outflow, the total volume of water in the soil column per surface area,

$$\mathcal{V} = \int_0^{L_z} \theta(h(z, t)) \, dz, \quad (B8)$$

increases, eventually leading to a rise of the groundwater table H over time.

In order to find the exact rate of change of $H(x, t)$, one should solve (B1) and find $H(x, t)$ for which $h_g(x, z = H(x, t), t) = 0$. Using the chain rule, we have

$$\frac{\partial}{\partial t} h_g(z = H(x, t), t) = \frac{\partial h_g(x, z, t)}{\partial z} \Big|_{z=H(x,t)} \frac{\partial H(x, t)}{\partial t} + \frac{\partial h_g}{\partial t} \Big|_{z=H(x,t)} = 0, \quad (B9)$$

from which the groundwater growth rate is

$$\frac{\partial H(x, t)}{\partial t} = - \left(\frac{\partial h_g(x, z, t)}{\partial z} \right)^{-1} \frac{\partial h_g}{\partial t} \Big|_{z=H(x,t)}. \quad (B10)$$

However, rather than solving Richards equation in the unsaturated zone, a standard time-dependent Boussinesq-based approach to groundwater modelling is based on introducing a drainable porosity defined as

$$f \equiv \frac{d\mathcal{V}}{dH}. \quad (B11)$$

In essence, the drainable porosity describes, for a given change in the height H , the corresponding change in the subsurface water volume \mathcal{V} (B8). It is often assumed that the drainable porosity f is a constant parameter characterising a given soil. However, as we

argue in [Appendix C](#), this assumption is not consistent with the Richards-based approach, in which the growth of the volume \mathcal{V} does not have to immediately lead to a rise in the groundwater volume. Therefore, in the same appendix, we introduce a mean drainable porosity $f(x)$, which does not fully represent the dynamics governed by the Richards equation but still allows us to exactly reproduce the time when the groundwater reaches the surface in the Richards-based approach.

Since the volume of subsurface water changes as a result of precipitation $r(x, t)$ and inflow/outflow q_z^{top} , we have

$$f(x) \frac{\partial H}{\partial t} = \frac{d\mathcal{V}}{dt} = q_z^{top} + r(x, t). \quad (\text{B12})$$

Substituting [\(B7\)](#) into the above expression gives us the governing equation for H :

$$f(x) \frac{\partial H}{\partial t} = K_s \frac{\partial}{\partial x} \left(HS_x + H \frac{\partial H}{\partial x} \right) + r(x, t). \quad (\text{B13})$$

This equation is equivalent to [\(2.3\)](#) under the additional assumptions that infiltration is equal to precipitation: as in Part 2, we ignore the effects of evapotranspiration and, in addition, we assume that no overland flow is generated unless the soil becomes fully saturated (i.e. rainfall never exceeds soil infiltration capacity, $r(x, t) \leq K_s$).

B.2. Region B: governing equation for seepage zone $H \geq 1$

In the case of the seepage zone, the groundwater height is fixed at $H_g = L_z$. However, we need to determine the additional surface water height, $h_s(x, t)$, which is given by solving the Saint Venant equation (see [\(3.3\)](#) from Part 2):

$$\frac{\partial h_s}{\partial t} = \frac{\partial}{\partial x} [Q_s(h_s)] + r(x, t) - I(x, t), \quad (\text{B14})$$

where the surface flow, $Q_s(h_s)$, is given by the Manning's equation [\(2.6\)](#), and I is the infiltration rate, equal to the negated vertical flow, $-q_z$, at ground level.

To determine the vertical flow, q_z , we perform a similar conservation argument as in [Appendix B.1](#). First, at the interface between the subsurface and surface flows, we set continuity of pressure and flow. The first condition allows us to specify the pressure head, h_g , at the surface:

$$h_g(x, z, t) = h_s(x, t) \quad \text{at } z = S_x x + L_z. \quad (\text{B15})$$

Consequently, we set the integration constant H , appearing in [\(B3\)](#), to $H(x, t) = L_z + h_s(x, t)$. Substituting it into [\(B4\)](#), we obtain

$$q_x = -K_s \left(S_x + \frac{\partial h_s}{\partial x} \right) \quad \text{for } 0 < z < L_z. \quad (\text{B16})$$

Now, let us consider the control volume of groundwater contained in the vertical column $[x, x + \Delta x]$, as illustrated in [figure 11](#) in region B. In this case, we have $H_g = L_z$, and the

mass balance equation (B7) yields

$$q_z|_{z=S_x x+L_z} = -L_z \frac{\partial q_x}{\partial x} = \frac{\partial}{\partial x} \left(K_s L_z S_x + K_s L_z \frac{\partial h_s}{\partial x} \right) = \frac{\partial}{\partial x} \left(K_s L_z \frac{\partial h_s}{\partial x} \right), \quad (\text{B17})$$

after substituting the expression (B16) for the groundwater flow, q_x . Thus, we have the required expression for the infiltration rate:

$$I(x, t) = -q_z|_{z=S_x x+L_z} = -\frac{\partial}{\partial x} \left(K_s L_z \frac{\partial h_s}{\partial x} \right). \quad (\text{B18})$$

Note that the infiltration is positive if surface water infiltrates into the soil or negative if groundwater emerges to the surface.

By substituting Q_s from (2.6) and infiltration I from (B18) into (B14), we obtain

$$\frac{\partial h_s}{\partial t} = \frac{\partial}{\partial x} \left(K_s L_z \frac{\partial h_s}{\partial x} + \frac{\sqrt{S_x}}{n_s} h_s^k \right) + r(x, t). \quad (\text{B19})$$

Note that in the seepage zone, $H = H_g + h_s$, where $H_g = L_z$ is constant. Hence, this equation is equivalent to the governing equation (2.5). Thus, we have derived both cases of the governing equation (2.7), forming the basis of this work.

Appendix C. Mean drainable porosity function, $f(x)$

C.1. On the mean drainable porosity

In Appendix B, we defined the drainable porosity f as the volumetric change in the subsurface volume for a given change in the groundwater height, dV/dH . However, this approach is not fully consistent with the solution for the Richards equation for subsurface flow.

Typically, in scenarios where the precipitation increases to a constant value $r > 1$, a characteristic wetting front is observed. This front can be seen in figure 8(d) in Part 2, and its propagation is discussed in detail by Caputo & Stepanyants (2008). The front moves downward towards the groundwater table, changing soil saturation and eventually leading to the rise of the groundwater table. This behaviour is not captured by a standard time-dependent Boussinesq equation or our 1-D model.

However, our analysis in §§ 6.1 and 6.2 shows that the most important mechanism by which groundwater contributes to the peak flow generation is by extending the seepage zone. Moreover, in Appendix F, we show that horizontal groundwater flow is negligibly slow and does not affect the speed at which the groundwater is rising over a short timescale characterising a typical rainfall. This means that the groundwater becomes saturated when rainwater fills the available drainable volume v_h , i.e. after time $t = v_h/r$. The same time is predicted by the 1-D model by setting an x -dependent mean drainable porosity $f(x)$, defined as

$$f(x) = \frac{v_H(x)}{D(x)}, \quad (\text{C1})$$

where $D(x)$ is the thickness of the unsaturated soil layer. The above choice of mean drainable porosity is the one that we use throughout this work.

To summarise, even though setting a time-independent porosity and constant groundwater recharge does not capture the delay required for the wetting front to reach the groundwater, it allows for the correct prediction of the soil critical time and the resultant peak flows observed in this work. In this model, note that $H(x, t)$ does not represent

the exact thickness of the saturated zone that forms groundwater but corresponds to the amount of water absorbed by the soil, even if it has not yet reached the saturated zone. However, this difference in interpretation does not seem to affect the main results obtained in this paper. Formulating this complex system in terms of a 1-D partial differential equation facilitates the analysis and computation.

C.2. Computation of mean drainable porosity

Here, we formally derive an expression for the mean porosity given the 1-D model parameters for the considered benchmark scenario. First, following the Richards equation, we find the pressure head h_g profile above the groundwater table and use it to evaluate the drainable volume for a column of soil of height $D(x)$ above the groundwater table.

We note that in the considered case of $\beta_{zx} = L_z/L_x \ll 1$, the leading solution of the 2-D Richards equation involves only vertical flow along the \hat{z} axis, as given by (B1). In the scenario considered in this paper, we assume that the system is initially in a steady state for a constant rainfall r_0 . Under these assumptions, we integrate the time-independent version of (B1) to form a first-order nonlinear ODE for the pressure head $h_g(\hat{z})$:

$$K_r(h_g) \left(\frac{dh_g}{d\hat{z}} + 1 \right) = \frac{r_0}{K_s}, \tag{C2}$$

where the constant of integration on the right-hand side has been chosen to match the dimensionless infiltration r_0/K_s , passing through the surface. Let us consider a column of the soil above a groundwater table, and we take $h_g|_{\hat{z}=0} = 0$. Given the pressure head, we can find the saturation $\theta(h_g(\hat{z}))$ following the Mualem–van Genuchten model:

$$\theta(h_g) = \begin{cases} \theta_r + \frac{\theta_s - \theta_r}{(1 + (\alpha h_g)^n)^m} & h_g < 0, \\ \theta_s & h_g \geq 0, \end{cases} \tag{C3}$$

where θ_s and θ_r are the saturated and residual water content, whereas α , n and $m = 1 - 1/n$ are other Mualem–van Genuchten parameters characterising a given soil. We can use (C3) to compute the drainable volume and resulting mean drainable porosity (C1):

$$f(x) = \frac{v_H(x)}{D(x)} = \frac{1}{D(x)} \int_0^{D(x)} [\theta_s - \theta(h_g(\hat{z}))] d\hat{z}. \tag{C4}$$

Solving (C2) and then numerically integrating (C4) allows us to calculate f .

C.3. Analytical approximations of mean drainable porosity

As an alternative to the integral expression above, let us develop an approximation for v_H , based on the assumption that the groundwater table is located near the land surface. Since for $h \rightarrow 0$, $K_r(h) \rightarrow 1$, the leading-order solution for (C2) around $\hat{z} = 0$ satisfies

$$h_g(\hat{z}) \sim \left(\frac{r_0}{K_s} - 1 \right) \hat{z}. \tag{C5}$$

Then, integrating (C4) with the Mualem–van Genuchten model (C3) gives

$$f_1(x) = (\theta_s - \theta_r) \left[{}_2F_1 \left(m, \frac{1}{n}; 1 + \frac{1}{n}; \left(-a \left(\frac{r_0}{K_s} - 1 \right) D(x) \right)^n \right) - 1 \right], \tag{C6}$$

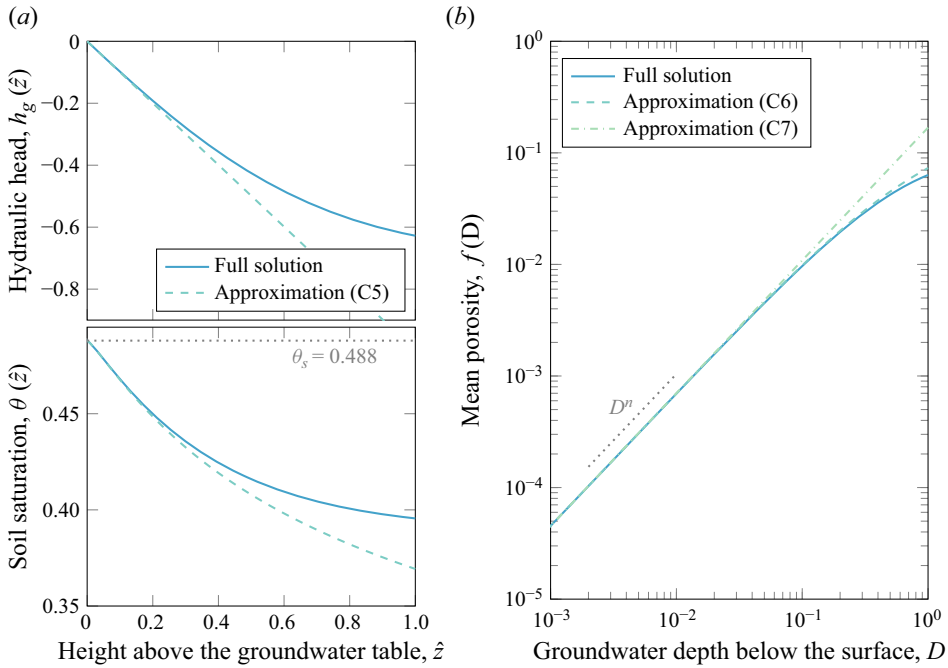


Figure 12. (a) Initial vertical profile of the pressure head h_g and corresponding saturation θ in a column of soil. (b) Dependence of mean porosity $f = v_h/D$ on the depth of the groundwater below the surface. As shown, approximations (C5)–(C7) accurately describe soil properties close to the groundwater table. We used Mualem–van Genuchten parameter values from the previous part of our work, i.e. $\alpha = 3.367 \text{ m}^{-1}$, $\theta_s = 0.388$, $\theta_R = 0.115$ and $n = 1.282$.

where ${}_2F_1$ is a hypergeometric function. One can also find the leading-order approximation of (C6) for $D \ll 1$, which yields

$$f_2(x) = \frac{m}{n+1}(\theta_s - \theta_r) \left[-\left(\frac{r_0}{K_s} - 1\right) \alpha D(x) \right]^n. \tag{C7}$$

However, the approximation (C6) is more accurate. Functions (C6) and (C7) are compared with the full numerical solution in figure 12.

Appendix D. Derivation of steady-state overland flow for $\mu \rightarrow \infty$

The steady state for the seepage zone is given by (5.1b):

$$1 + \sigma \frac{\partial h_0}{\partial x} + \mu h_0^k = \rho_0(1 - x), \tag{D1}$$

where we used $h_0(x) = H(0) - 1$ to represent the surface water height.

As we have noted previously, our regime of interest is where μ is large. It is convenient to rescale via $x = aX$, where a was defined as the size of the seepage zone, so that the domain is fixed in $X \in [0, 1]$. In the limit $\mu \rightarrow \infty$, we anticipate from dominant balance that the overland flow is small, $h_0 \rightarrow 0$, and hence we rescale $h_0 = \mu^{-1/k}g(X)$ in order to balance the third term with the right-hand side of (D1). With the boundary conditions (4.3a,c), this

rescaling gives

$$\frac{Pe^{-1}}{a} \frac{\partial g}{\partial X} + g^k = \rho_0(1 - aX) - 1, \tag{D2a}$$

$$g'(0) = 0 \quad \text{and} \quad g(1) = 0. \tag{D2b}$$

In (D2a), for convenience, we have defined the small parameter

$$Pe^{-1} = \frac{\sigma}{\mu^{1/k}} \ll 1, \tag{D3}$$

which, according to table 1, is approximately $Pe^{-1} \approx 10^{-5}$. As we show, the asymptotic analysis as $Pe^{-1} \rightarrow 0$ involves the analysis of an outer solution, where $0 \leq X < 1$, and an inner solution with a boundary layer, where $X \rightarrow 1$.

In the outer region, we expand the solution and contact line as

$$g(X) = g_0(X) + Pe^{-1}g_1(X) + \dots \quad \text{and} \quad a = a_0 + Pe^{-\gamma}a_1 + \dots, \tag{D4}$$

where $\gamma > 0$ and is to be determined later. Then we develop the following leading-order approximation of the outer surface water height via (D2a),

$$g(X) \sim g_0(X) = [\rho_0(1 - a_0X) - 1]^{1/k}. \tag{D5}$$

The above outer expansion exhibits an infinite gradient, possibly before the contact line is reached, at the point $X = (1 - \rho_0^{-1})/a_0$. However, we show in the following that a_0 is such that this point corresponds to $X = 1$.

In order to develop the solution within the boundary layer, we consider rescaling

$$g(X) = Pe^{-\beta} \hat{G}(\hat{X}) \quad \text{and} \quad X = 1 - Pe^{-\alpha} \hat{X}, \tag{D6}$$

with α , β and γ from (D4) to be determined. Applying these transformations to (D2a) gives

$$\begin{aligned} & Pe^{-(1+\beta-\alpha)} \left[-\frac{1}{a_0} \frac{\partial \hat{G}}{\partial \hat{X}} \right] + Pe^{-k\beta} [\hat{G}^k] \\ & = [\rho_0(1 - a_0) - 1] + Pe^{-\alpha} [\rho_0 a_0 \hat{X}] - Pe^{-\gamma} [\rho_0 a_1] + o(Pe^{-\alpha}). \end{aligned} \tag{D7}$$

The balance of Pe terms is achieved for $1 + \beta - \alpha = k\beta = \alpha = \gamma$, which corresponds to $\alpha = \gamma = k/(2k - 1)$ and $\beta = 1/(2k - 1)$. Equation (D7) for the leading $O(1)$ term is $\rho_0(1 - a_0) - 1 = 0$, and hence this approximation gives us an estimate for the leading-order contact line position,

$$a \sim a_0 = 1 - \frac{1}{\rho_0}. \tag{D8}$$

Indeed, this equation confirms that the leading-order outer solution, (D5), predicts an infinite gradient as $X \rightarrow 1$. In order to derive an approximation for the gradient of the surface water height near the contact line, we must proceed to the next order in the inner region.

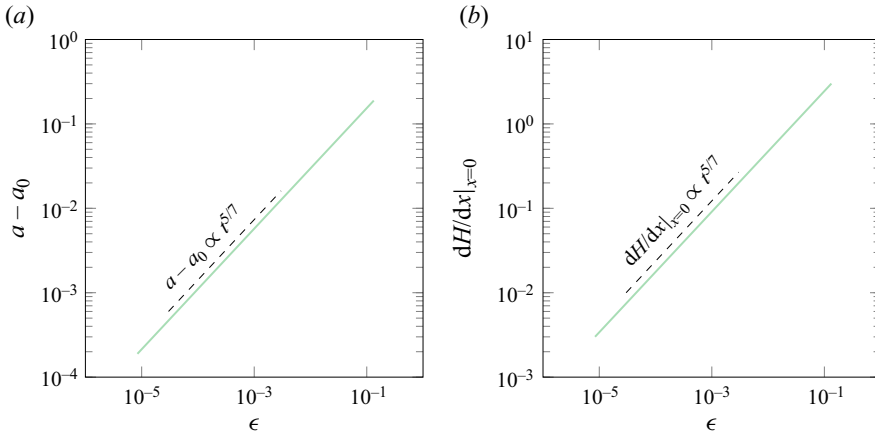


Figure 13. (a) The size of the seepage zone relative to its first-order approximation $a - a_0$. (b) The gradient of H at this point. The results were obtained by solving (D1). The fitted power law is consistent with the theoretical exponent $\gamma = 5/7$.

Equation (D7) at $O(Pe^{-k/(2k-1)})$ yields

$$-\frac{1}{a_0} \frac{\partial \hat{G}}{\partial \hat{X}} + \hat{G}^k = \rho_0 a_0 \hat{X} - \rho_0 a_1, \tag{D9a}$$

along with the two boundary conditions:

$$\hat{G}(0) = 0 \quad \text{and} \quad \hat{G}(\hat{X} \rightarrow \infty) \sim (\rho_0 - 1)^{1/k} \hat{X}^{1/k}. \tag{D9b}$$

The second boundary condition above corresponds to the inner limit of the outer solution (D5). The above first-order ODE, together with the two boundary conditions, forms a boundary value problem with eigenvalue a_1 . It cannot be solved analytically. In any case, if desired, the above problem can be computed numerically, and it would yield the correction to the contact line, $a_1 = a_1(\rho_0)$.

Note finally that the gradient of h_0 at $x = a$ can now be estimated directly from (D1). Since $h_0(a) = 0$, we have, using the expansion (D4),

$$\left. \frac{\partial h_0}{\partial x} \right|_{x=a} = \frac{\rho_0(1-a) - 1}{\sigma} \sim \frac{\rho_0(1-a_0) - 1 - \rho_0 a_1 Pe^{-\gamma}}{\sigma} = -\frac{\rho_0 a_1}{\sigma} Pe^{-\gamma}. \tag{D10}$$

For Manning’s law, $k = 5/3$, so $\gamma = k/(2k - 1) = 5/7$. Hence, we expect the gradient to be $dh_0/dx = O(Pe^{-5/7})$ while the contact line position equally satisfies $a - a_0 = O(Pe^{-5/7})$. These two scaling laws are confirmed by solving the boundary value problem given by (D2a) numerically and transforming it back to the original variables (see figure 13).

Appendix E. Derivation of the initial groundwater table for $\sigma \rightarrow 0$

Here, we find the leading-order solution for the ODE (5.6) under the limit $\epsilon = \sigma \rightarrow 0$:

$$\epsilon \frac{dH_0}{dx} = \frac{\rho_0(1-x)}{H_0(x)} - 1, \quad \text{for } x \in [a_0, 1], \tag{E1}$$

with a boundary condition $H_0(a_0) = 1$, and where $a(t) \sim a_0$ is the leading-order contact line position as $Pe \rightarrow \infty$. Expanding H_0 in powers of ϵ , we obtain the approximation:

$$H_0(x) = \rho_0(1 - x) + \rho_0\epsilon + O(\epsilon^2). \tag{E2}$$

This solution does not satisfy the boundary condition at $x = a_0$. For $x \rightarrow a_0$, we develop an inner expansion by re-scaling $x = a_0 + \epsilon X$ and $H_0(x) = g(X)$. The ODE now becomes

$$\frac{dg}{dX} = \frac{\rho_0(1 - a_0 - \epsilon X)}{g(X)} - 1, \quad \text{for } X > 0, \tag{E3}$$

with $g(0) = 1$. Solving now to the first two orders, we have

$$g(X) = 1 + \epsilon\rho_0(1 - e^{-X} - X) + O(\epsilon^2), \tag{E4}$$

where we have used $a_0 = 1 - 1/\rho_0$ from (5.5).

The composite solution is obtained by adding the outer and inner asymptotic expansions from (E2) and (E4), respectively, and subtracting their common part. The final result, to two orders of accuracy, is the following approximation:

$$H_0(x) = \rho_0(1 - x + \epsilon - \epsilon e^{-(x-a_0)/\epsilon}) + O(\epsilon^2). \tag{E5}$$

After replacing ϵ with σ , we obtain the solution (5.7) stated in the main text.

Appendix F. Derivation of the time-dependent groundwater solution for $t \rightarrow 0$ and $\rho \rightarrow \infty$

We provide additional details for the early-time analysis of § 6.1, particularly in connection with the boundary-layer asymptotics. Consider (4.3b) outside the seepage zone ($H < 1$):

$$f(x)\frac{\partial H}{\partial t} = \frac{\partial}{\partial x} \left(\sigma H \frac{\partial H}{\partial x} + H \right) + \rho. \tag{F1}$$

As noted in § 6.1, we consider the initial condition, $H(x, t = 0) = H_0(x; \rho_0)$, to be the steady-state response of the system to a precipitation rate, ρ_0 . That is, the initial groundwater solution satisfies (5.6):

$$(\sigma H_0 H_0' + H_0)' + \rho_0 = 0, \tag{F2}$$

subject to the boundary conditions (4.3b,d) in § 5, i.e.

$$H(x = a(t)) = 1 \quad \text{and} \quad \left(\sigma H \frac{\partial H}{\partial x} + H \right) \Big|_{x=1} = 0. \tag{F3}$$

Let us consider the short-time behaviour of the time-dependent equation. Let $t = \epsilon t'$, $H(x, t) = H_0(x) + \epsilon H'(x, t)$, where $\epsilon \ll 1$. Then, (F1) becomes

$$f(x)\frac{\partial H'}{\partial t'} = \rho - \rho_0 + \epsilon \frac{\partial}{\partial x} \left(\sigma H_0 \frac{\partial H'}{\partial x} + \sigma H' \frac{\partial H_0}{\partial x} + H' \right) + O(\epsilon^2). \tag{F4}$$

Therefore, the first two leading terms of the small-time groundwater solution are

$$H(x, t) = H_0(x; \rho_0) + \left[\frac{\Delta\rho}{f(x)} \right] t + O(t^2), \quad \text{as } t \rightarrow 0 \text{ with } x > a(t), \tag{F5}$$

where $\Delta\rho \equiv \rho - \rho_0$. Thus, we see that (F5) predicts that the groundwater height increases linearly with time by an amount proportional to the sudden impulse of rain (or, rather, its difference $\Delta\rho$).

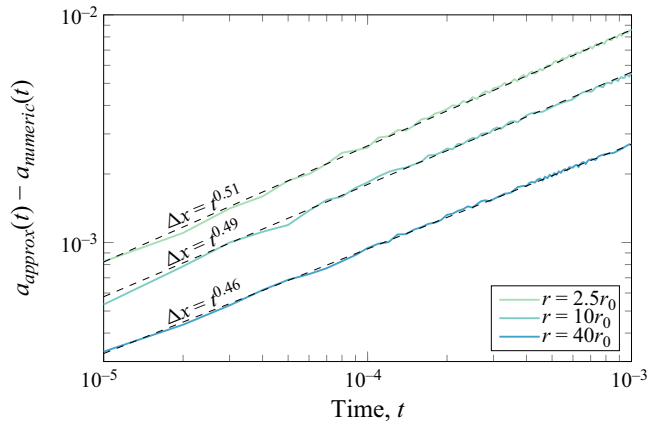


Figure 14. Difference between the location of the seepage front obtained by solving PDE (2.8a) and obtained using the leading-term outer solution (F5) for rainfalls with three different precipitation rates.

However, the above asymptotic solution assumes that $x - a(t) = O(1)$, and indeed it fails to account for the fact that $H = 1$ when $x = a(t)$. We must consider it to be an *outer* solution, valid away from $x = a(t)$. A comparison between the outer approximation (F5) and the full solution is shown in figure 7(a). In the case of the fully coupled surface–subsurface flow, the solution of the PDE diverges from the outer solution (F5) within a small boundary layer around the seepage front.

The size of the boundary layer tends to zero as $\rho \rightarrow \infty$. This is tested as follows. First, we compute the full PDE model (2.8a) and find the place where $H(x_{numeric}) = 1$. Then, we estimate the boundary layer thickness by finding the difference between $x_{numeric}$ and $x_{approx} = 1 - 1/\rho$, which is the leading-order (outer) approximation of $a(t)$. As figure 14 demonstrates, it depends both on time t and precipitation represented by ρ .

The above is confirmed via a dominant balance. Let $x = a + \delta x'$. Then (F4) becomes

$$f(x) \frac{\partial H'}{\partial t'} = \rho - \rho_0 + \frac{\epsilon}{\delta^2} \frac{\partial}{\partial x'} \left(\sigma H_0 \frac{\partial H'}{\partial x'} + \sigma H' \frac{\partial H_0}{\partial x'} + \delta H' \right) + O(\epsilon^2). \quad (F6)$$

The diffusion terms become significant and balance the precipitation ρ when $\epsilon/\delta^2 \sim \Delta\rho$. Then the thickness of the boundary layer is on the order of $\delta = \epsilon^{1/2} \Delta\rho^{-1/2}$, i.e. it increases proportionally to $t^{1/2}$ and $\Delta\rho^{-1/2}$. These trends are confirmed in figure 14.

Appendix G. Derivation of the explicit solution for $Q(t)$

In this appendix, we show that the implicit solution (6.16) for late time (i.e. for $Q_s^* > \rho a_0$),

$$t^*(Q_s^*) = \frac{1}{\rho} (Q_s^*)^{1/k} + \mu^{1/k} \mathcal{T} \left(\frac{Q_s^*}{\rho} \right), \quad (G1)$$

can be written in an explicit form given by (6.18a–c), as long as the increase of flow after the critical time is negligibly small compared with the critical flow value $Q_{crit} = \rho a_0$. This assumption is motivated by the observation that the dynamics of the flow increase after reaching critical flow slows down significantly.

Asymptotic analysis of catchment models. Part 3

Let us consider the flow Q_s^* near its critical value, $Q_s^* = \rho a_0 + \epsilon Q'$, and consider the asymptotic limit $\epsilon \rightarrow 0$. Then (G1) becomes

$$t^* = \frac{1}{\rho}(\rho a_0 + \epsilon Q')^{1/k} + \mu^{1/k} \mathcal{T}(Q_s^*). \tag{G2}$$

Therefore, we have

$$t^* = \underbrace{\frac{1}{\rho}(\rho a_0)^{1/k}}_{t_{crit}} + \mu^{1/k} \mathcal{T}(Q_s^*) + O(\epsilon). \tag{G3}$$

By neglecting the $O(\epsilon)$ term, we get

$$t^* - t_{crit} = \mu^{1/k} \mathcal{T}(Q_s^*), \tag{G4}$$

which allows us to obtain an explicit equation for Q_s^* :

$$Q_s^* = \mathcal{T}^{-1}(\mu^{-1/k}(t^* - t_{crit})). \tag{G5}$$

Now we need to find an inverse function for $t = \mathcal{T}(a(t))$, i.e. a function that provides the location of the seepage front for a given time. Function \mathcal{T} is defined by (6.2) as

$$\mathcal{T}(x = a(t)) \sim \frac{f(x = a(t))}{\rho - \rho_0} (1 - H_0(x = a(t))). \tag{G6}$$

We use the approximation of $f(x)$ given by (C7), and the approximation of $H(x)$ given by (5.7),

$$f(x) = CD(x)^n, \quad \text{where } C = \frac{m}{n+1}(\theta_s - \theta_r) \left[- \left(\frac{r_0}{K_s} - 1 \right) \alpha \right]^n, \tag{G7a}$$

$$D(x) = 1 - H(x) = 1 - \rho_0(1 - x + \sigma - \sigma e^{-(x-a_0)/\sigma}). \tag{G7b}$$

By substituting (G7a) to (G6) we obtain

$$\mathcal{T}(x = a(t)) = \frac{1}{\rho - \rho_0} CD(x = a(t))^{n+1}. \tag{G8}$$

Now, we solve this equation for $D(x = a(t))$:

$$[C^{-1}(\rho - \rho_0)\mathcal{T}(x = a(t))]^{1/(n+1)} = D(x = a(t)). \tag{G9}$$

After substituting (G7b) we get

$$\rho s(t) = A \rho t^{1/(n+1)} = 1 - \rho_0(1 - x + \sigma - \sigma e^{-(x-a_0)/\sigma}), \tag{G10}$$

where we introduced $A = [C^{-1}(\rho - \rho_0)]^{1/(n+1)}$ and $t = \mathcal{T}(x = a(t))$ to shorten the notation. The solution of this equation for x is

$$x = a(t) = s(t) + \underbrace{\sigma + 1}_{a_0} - \frac{1}{\rho_0} + \sigma W_0(-e^{-1-s(t)/\sigma}), \tag{G11}$$

where $W_0(\cdot)$ is the Lambert W function. Therefore, the solution can be written as

$$a(t) = \underbrace{a_0}_{term1} + \underbrace{s(t)}_{term2} + \underbrace{\sigma[1 + W_0(-e^{-1-s(t)/\sigma})]}_{term3}. \tag{G12}$$

This concludes the derivation of the explicit solution (6.18). The accuracy of this approximation is demonstrated in figure 9.

REFERENCES

- ABDUL, A.S. & GILLHAM, R.W. 1989 Field studies of the effects of the capillary fringe on streamflow generation. *J. Hydrol.* **112** (1–2), 1–18.
- ANDERSON, M.G. & BROOKS, S. 1996 *Advances in Hillslope Processes*, vol. 1. Wiley.
- BARTLETT, M.S. & PORPORATO, A. 2018 A class of exact solutions of the Boussinesq equation for horizontal and sloping aquifers. *Water Resour. Res.* **54** (2), 767–778.
- BATHURST, J.C., EWEN, J., PARKIN, G., O'CONNELL, P.E. & COOPER, J.D. 2004 Validation of catchment models for predicting land-use and climate change impacts. 3. Blind validation for internal and outlet responses. *J. Hydrol.* **287** (1–4), 74–94.
- BEAR, J. & VERRUIJT, A. 1987 *Modeling Groundwater Flow and Pollution*, vol. 2. Springer Science & Business Media.
- BEDIENT, P.B., HUBER, W.C. & VIEUX, B.E. 2008 *Hydrology and Floodplain Analysis*, vol. 816. Prentice Hall.
- BELL, V.A., KAY, A.L., JONES, R.G. & MOORE, R.J. 2007 Development of a high resolution grid-based river flow model for use with regional climate model output. *Hydrol. Earth Syst. Sci.* **11** (1), 532–549.
- BEVEN, K. 2018 On hypothesis testing in hydrology: why falsification of models is still a really good idea. *Wiley Interdiscip. Rev.: Water* **5** (3), e1278.
- BEVEN, K. 2019 How to make advances in hydrological modelling. *Hydrol. Res.* **50** (6), 1481–1494.
- BEVEN, K. & GERMANN, P. 2013 Macropores and water flow in soils revisited. *Water Resour. Res.* **49** (6), 3071–3092.
- BOUSSINESQ, J. 1877 *Essai sur la théorie des eaux courantes*. Imprimerie nationale.
- CAPUTO, J.-G. & STEPANYANTS, Y.A. 2008 Front solutions of Richards' equation. *Transp. Porous Media* **74** (1), 1–20.
- COOK, F.J., KNIGHT, J.H. & WOODING, R.A. 2009 Steady groundwater flow to drains on a sloping bed: comparison of solutions based on Boussinesq equation and Richards equation. *Transp. Porous Media* **77** (2), 357–372.
- CUNNANE, C. 1987 Review of statistical models for flood frequency estimation. In *Hydrologic Frequency Modeling: Proceedings of the International Symposium on Flood Frequency and Risk Analyses, 14–17 May 1986, Louisiana State University, Baton Rouge, USA*, pp. 49–95. Springer.
- DUPUIT, J. 1863 *Études théoriques et pratiques sur le mouvement des eaux dans les canaux découverts et à travers les terrains perméables: avec des considérations relatives au régime des grandes eaux, au débouché à leur donner, et à la marche des alluvions dans les rivières à fond mobile*. Dunod.
- FORCHHEIMER, P. 1914 *Hydraulik*. BG Teubner.
- GRAYSON, R.B., MOORE, I.D. & MCMAHON, T.A. 1992 Physically based hydrologic modeling: 2. Is the concept realistic? *Water Resour. Res.* **28** (10), 2659–2666.
- GUÉRIN, A., DEVAUCHELLE, O. & LAJEUNESSE, E. 2014 Response of a laboratory aquifer to rainfall. *J. Fluid Mech.* **759**, R1.
- GUSTARD, A., BULLOCK, A. & DIXON, J.M. 1992 *Low Flow Estimation in the United Kingdom*. Institute of Hydrology.
- HÁLEK, V. & ŠVEC, J. 2011 *Groundwater Hydraulics*. Elsevier.
- HENDERSON, F.M. & WOODING, R.A. 1964 Overland flow and groundwater flow from a steady rainfall of finite duration. *J. Geophys. Res.* **69** (8), 1531–1540.
- HORTON, R.E. 1936 Maximum ground-water levels. *Eos, Trans. Am. Geophys. Union* **17** (2), 344–357.
- KIRKBY, M.J. 2019 Infiltration, throughflow, and overland flow. In *Introduction to Physical Hydrology* (ed. R.J. Chorley), pp. 109–120. Routledge.
- KIRKBY, M.J. & BEVEN, K.J. 1979 A physically based, variable contributing area model of basin hydrology. *Hydrol. Sci. J.* **24** (1), 43–69.
- KJELSDEN, T.R., JONES, D.A. & BAYLISS, A.C. 2008 *Improving the FEH Statistical Procedures for Flood Frequency Estimation*. Environment Agency.
- KLEMES, V. 1986 Operational testing of hydrological simulation models. *Hydrol. Sci. J.* **31** (1), 13–24.
- KOLLET, S., *et al.* 2017 The integrated hydrologic model intercomparison project, IH-MIP2: a second set of benchmark results to diagnose integrated hydrology and feedbacks. *Water Resour. Res.* **53** (1), 867–890.
- LAMB, R. 1999 Calibration of a conceptual rainfall-runoff model for flood frequency estimation by continuous simulation. *Water Resour. Res.* **35** (10), 3103–3114.
- MACDONALD, I., BAINES, M.J., NICHOLS, N.K. & SAMUELS, P.G. 1995 Comparison of some steady state Saint-Venant solvers for some test problems with analytic solutions. *Numer. Anal. Rep.* **2**, 95.
- MAXWELL, R.M., *et al.* 2014 Surface-subsurface model intercomparison: a first set of benchmark results to diagnose integrated hydrology and feedbacks. *Water Resour. Res.* **50** (2), 1531–1549.
- MIZUMURA, K. 2002 Drought flow from hillslope. *J. Hydrol. Engng* **7** (2), 109–115.

Asymptotic analysis of catchment models. Part 3

- MOORE, R.J. 2007 The PDM rainfall-runoff model. *Hydrol. Earth Syst. Sci.* **11** (1), 483–499.
- MOORE, R.J., BELL, V.A., COLE, S.J. & JONES, D.A. 2007 Rainfall-runoff and other modelling for ungauged/low-benefit locations. *Tech. Rep.*, CEH Wallingford, Environment Agency, Bristol, UK.
- MORAWIECKI, P.W. 2022 GitHub repository for 3D, 2D and 1D benchmark catchment models. <https://github.com/Piotr-Morawiecki/benchmark-catchment-model>.
- MORAWIECKI, P.W. 2023 An asymptotic framework for the comparison and analysis of flood estimation models. PhD thesis, University of Bath.
- MORAWIECKI, P.W. & TRINH, P.H. 2023a A calibration-free physicality-based model for predicting peak river flows. Preprint [arXiv:2401.05349](https://arxiv.org/abs/2401.05349).
- MORAWIECKI, P.W. & TRINH, P.H. 2023b Asymptotic differences between a lumped probability-distributed rainfall-runoff model and a physical benchmark model. Preprint [arXiv:2312.01371](https://arxiv.org/abs/2312.01371).
- MORAWIECKI, P.W. & TRINH, P.H. 2023c On the evaluation of grid and grid-to-grid rainfall-runoff models and their differences with physical benchmarks. Preprint [arXiv:2312.01372](https://arxiv.org/abs/2312.01372).
- MORAWIECKI, P.W. & TRINH, P.H. 2024a On the development and analysis of coupled surface–subsurface models of catchments. Part 1. Analysis of dimensions and parameters for uk catchments. *J. Fluid Mech.* **982**, A28.
- MORAWIECKI, P.W. & TRINH, P.H. 2024b On the development and analysis of coupled surface–subsurface models of catchments. Part 2. A three-dimensional benchmark model and its properties. *J. Fluid Mech.* **982**, A29.
- PANICONI, C., TROCH, P.A., VAN LOON, E.E. & HILBERTS, A.G.J. 2003 Hillslope-storage Boussinesq model for subsurface flow and variable source areas along complex hillslopes: 2. Intercomparison with a three-dimensional Richards equation model. *Water Resour. Res.* **39** (11). doi:10.1029/2002WR001730.
- PARKIN, G., O'DONNELL, G., EWEN, J., BATHURST, J.C., O'CONNELL, P.E. & LAVABRE, J. 1996 Validation of catchment models for predicting land-use and climate change impacts: 2. Case study for a Mediterranean catchment. *J. Hydrol.* **175** (1–4), 595–613.
- PARLANGE, J.-Y., ROSE, C.W. & SANDER, G. 1981 Kinematic flow approximation of runoff on a plane: an exact analytical solution. *J. Hydrol.* **52** (1–2), 171–176.
- PARLANGE, J.-Y., STAGNITTI, F., HEILIG, A., SZILAGYI, J., PARLANGE, M.B., STEENHUIS, T.S., HOGARTH, W.L., BARRY, D.A. & LI, L. 2001 Sudden drawdown and drainage of a horizontal aquifer. *Water Resour. Res.* **37** (8), 2097–2101.
- PAUWELS, V.R.N. & UIJLENHOET, R. 2018 Confirmation of a short-time expression for the hydrograph rising limb of an initially dry aquifer using laboratory hillslope outflow experiments. *Water Resour. Res.* **54** (12), 10–350.
- PEEL, M.C. & MCMAHON, T.A. 2020 Historical development of rainfall-runoff modeling. *Wiley Interdiscip. Rev.: Water* **7** (5), e1471.
- POLIBARINOVA-KOCHINA, P. & WIEST, R.D. 1962 *Theory of Groundwater Movement*. Princeton University.
- SCUDELER, C., PANICONI, C., PASETTO, D. & PUTTI, M. 2017 Examination of the seepage face boundary condition in subsurface and coupled surface/subsurface hydrological models. *Water Resour. Res.* **53** (3), 1799–1819.
- SHAW, E., BEVEN, K., CHAPPELL, N. & LAMB, R. 2010 *Hydrology in Practice*, 3rd edn. CRC Press.
- SULIS, M., MEYERHOFF, S.B., PANICONI, C., MAXWELL, R.M., PUTTI, M. & KOLLET, S.J. 2010 A comparison of two physics-based numerical models for simulating surface water–groundwater interactions. *Adv. Water Resour.* **33** (4), 456–467.
- TAO, W., WANG, Q. & LIN, H. 2018 An approximate analytical solution for describing surface runoff and sediment transport over hillslope. *J. Hydrol.* **558**, 496–508.
- TRACY, F.T. 2006 Clean two- and three-dimensional analytical solutions of Richards' equation for testing numerical solvers. *Water Resour. Res.* **42** (8). doi:10.1029/2005WR004638.
- TROCH, P.A., *et al.* 2013 The importance of hydraulic groundwater theory in catchment hydrology: the legacy of Wilfried Brutsaert and Jean-Yves Parlange. *Water Resour. Res.* **49** (9), 5099–5116.
- TROCH, P.A., PANICONI, C. & EMIEL VAN LOON, E. 2003 Hillslope-storage Boussinesq model for subsurface flow and variable source areas along complex hillslopes: 1. Formulation and characteristic response. *Water Resour. Res.* **39** (11). doi:10.1029/2002WR001728.
- VIEIRA, J.H.D. 1983 Conditions governing the use of approximations for the Saint-Venant equations for shallow surface water flow. *J. Hydrol.* **60** (1–4), 43–58.
- WARRICK, A.W., LOMEN, D.O. & ISLAS, A. 1990 An analytical solution to Richards' equation for a draining soil profile. *Water Resour. Res.* **26** (2), 253–258.
- WOODING, R.A. & CHAPMAN, T.G. 1966 Groundwater flow over a sloping impermeable layer: 1. Application of the Dupuit–Forchheimer assumption. *J. Geophys. Res.* **71** (12), 2895–2902.
- WOOLHISER, D.A. & LIGGETT, J.A. 1967 Unsteady, one-dimensional flow over a plane: the rising hydrograph. *Water Resour. Res.* **3** (3), 753–771.